Statistical investigation of local strength and deformation of a shock wave interacting with turbulence

乱流と干渉した衝撃波の局所的な強さと変形に関する統計調査

Nagoya University
Graduate school of engineering
Department of aerospace engineering
Fluid dynamics laboratory

Tanaka Kento

Contents

List of figures

List of tables

List of achievements

Published papers

- K. Tanaka, T. Watanabe, K. Nagata, A. Sasoh, Y. Sakai, and T. Hayase. Amplification and attenuation of shock wave strength caused by homogeneous isotropic turbulence. *Phys. Fluids*, 30(3):035105, 2018.
- K. Tanaka, T. Watanabe, and K. Nagata. Statistical analysis of deformation of a shock wave propagating in a local turbulent region. *Phys. Fluids*, 32(9):096107, 2020.

International conferences

- K. Tanaka, T. Watanabe, K. Nagata, A. Sasoh, Y. Sakai, and T. Hayase. DNS study on shock/turbulence interaction in homogeneous isotropic turbulence at low turbulent Mach number. *69th Annual Meeting of the American Physical Society Division of Fluid Dynamics*, Portland, USA , 2016.
- K. Tanaka, T. Watanabe, K. Nagata, A. Sasoh, Y. Sakai, and T. Hayase. Direct numerical simulations of interaction between planar shock wave and homogeneous isotropic turbulence at low turbulent Mach number. *31st International Symposium on Shock Waves*, Nagoya, Japan, 2017.
- K. Tanaka, T. Watanabe, and K. Nagata. Effects of turbulence compressibility on normal shock wave in shock turbulence interactions. *32nd International Symposium on Shock Waves*, Singapore, 2019.
- K. Tanaka, T. Watanabe, and K. Nagata. Direct numerical simulations on ef-

fects of turbulent Mach number in interaction between planar shock wave and turbulence. *17th European Turbulence Conference*, Torino, Italy, 2019.

Nomenclature

t	: time
x_i	: position in i direction
x, y, z	: position
$\mathbf{u}$	: velocity vector
u_i	: velocity component in i direction
u, v, w	: velocity components in x, y, and z directions
ρ	: density
p	: pressure
T	: temperature
e	: total energy
γ	: specific heat ratio
R	: gas constant
a	: speed of sound
μ	: viscosity coefficient
ν	: kinematic viscosity
κ	: thermal conductivity
τ_{ij}	: shear stress tensor
S_{ij}	: rate-of-strain tensor ($S_{ij} \equiv (\partial u_i/\partial x_j + \partial u_j/\partial x_i)/2$)
W_{ij}	: rate-of-rotation tensor($W_{ij} \equiv (\partial u_i/\partial x_j - \partial u_j/\partial x_i)/2$)
δ_{ij}	: Kronecker delta
L_x, L_y, L_z	: computational domain size in each direction
N_x, N_y, N_z	: number of grid points in each direction

Δ	: computational grid size
L	: integral length scale
λ	: Taylor microscale
η	: Kolmogorov length scale
ε	: dissipation rate of turbulent kinetic energy ($\varepsilon \equiv \tau_{ij} S_{ij}$)
U_s	: propagation velocity of shock wave
θ	: dilatation ($\theta \equiv \nabla \cdot \mathbf{u}$)
θ_s	: dilatation at shock wave position
x_s	: shock wave position
$\overline{f}$	: plane average of f
$\langle f \rangle$	: volume average of f
f'	: fluctuations of f from average
f'_{rms}	: root-mean-squared (rms) value of fluctuations of variable f
M_s	: shock Mach number ($M_s \equiv U_s/a$)
M_t	: turbulent Mach number ($M_t \equiv \sqrt{3} u'_{rms}/a$)
Re_λ	: turbulent Reynolds number ($Re_\lambda \equiv u'_{rms}\lambda/\nu$)

Chapter 1

Introduction

1.1 Background and previous studies

An interaction between a shock wave and turbulence (hereafter denoted as "a shock–turbulence interaction") occurs in various phenomena across a wide range of scientific fields. Shock waves mainly appear in a supersonic flow and often interact with surrounding turbulence. For example, interactions between a shock wave and a turbulent boundary layer occur on the surface of high-speed airplanes. The interaction can induce flow separation due to an adverse pressure gradient past the shock wave and local high heating rates [1]. Shock waves have also been reported to interact with turbulence in supernova explosions [2], inertial confinement fusion [3], and sonic booms associated with supersonic flight [4].

Sonic booms present one of the biggest problems in engineering related to shock–turbulence interaction. Induced by shock waves generated by supersonic flight, a sonic boom is a loud noise that can adversely affect surrounding environments and ecosystems. The discontinuous pressure jumps produced by shock waves can cause damage like breaking glass windows. The shock waves generated by the Chelyabinsk meteor, for example, caused the windows in houses in Russia to shatter [5]. These loud noises can also influence the attitude and behavior of animals [6]. Therefore, it is necessary to develop a tool to predict sonic booms for the development and operation of future supersonic transport.

The effects of atmospheric turbulence on shock waves further complicate the sonic boom problem. The shock waves generated by supersonic flight interact with atmospheric turbulence in the propagation process, which changes their characteristics. It is reported that the pressure waveforms depend on the observation points in the flight test [4], and a recent study also suggests that the effects of the interaction should be considered for the sonic boom problem [7].

Previous studies of shock–turbulence interaction have investigated both turbulence and shock waves. Velocity fluctuations and enstrophy have been observed to amplify following interaction. In addition, characteristic length scales of turbulence are affected by the interaction due to the strong compression in the shock wave. These results have been observed in both experimental [8]–[10] and numerical [11]–[16] studies and agree well with theoretical analyses using linear interaction analysis (LIA) [17]–[22], rapid distortion theory (RDT) [23]–[25], and quasi-equilibrium assumption [15]. Conversely, a shock wave is also modulated by the interaction. Characteristics of a normal shock wave interacting with homogeneous isotropic turbulence (HIT) are investigated via direct numerical simulations (DNSs) [11], [15], [26], [27]. In these DNSs, the divergence of a velocity vector called a dilatation, which represents the strength of fluid compression, is used as a measure of the local shock strength. Shock–turbulence interactions have been reported to cause the dilatation of the shock wave to fluctuate. Discontinuous jumps in local areas of the shock wave disappear during the interaction in cases of high turbulent Mach numbers $M_t(\equiv \sqrt{3}u'_{rms}/a)$, where u'_{rms} is the root-mean-squared (rms) value of the velocity fluctuations, u', and a is the speed of sound in front of the shock wave. The shock wave whose discontinuity locally disappears is called a broken shock wave. The broken part of the shock wave can be observed in cases of $M_t/(M_s - 1) > 0.6$, where $M_s(\equiv U_s/a)$ is the shock Mach number, and U_s is the propagation velocity of the shock wave. Statistical characteristics of the fluctuations of pressure jumps across a shock wave have been reported in experimental studies [28]–[33]. Other reports have observed a correlation between the fluctuations of the pressure jumps and velocity fluctuations normal to the shock wave during turbulence. Here, a time lag called a finite response

time exists from the interaction with the velocity fluctuations until the shock wave is modulated [30], [33]. The correlation and the finite response time are explained based on the curvature of the shock-wave surface induced by the velocity shear [30]. However, no direct observation has been reported for the relation between the local shock-wave deformation and local velocity shear because of the difficulty in measuring the local curvature of the shock-wave surface in experiments.

According to previous studies, shock-wave deformation strongly relates to a local shock strength in a shock–turbulence interaction. Although the deformed shock wave has been visualized in numerical simulations [11], [12], [26], [27], the statistical characteristics of the deformation have not been investigated. Tamba *et al.* studied the shock-wave deformation in the interaction between a normal shock wave and grid turbulence in a counter-driver shock tube[34]. They reported that the shock-wave deformation started at the beginning of the interaction and increased with propagation distance in the turbulent region, called the interaction length. Prior numerical studies had not considered the effects of interaction length, so this study was the first to indicate the importance of the transient process of shock-wave deformation. However, the study did not investigate the statistical properties of the shock-wave deformation because of the limitations of the shadowgraph and schlieren visualizations used. This leaves a literature gap and opportunity for new studies to investigate the statistical characteristics of the shock-wave deformation and the effects of interaction length.

1.2 Objectives and structure of this thesis

As reported in previous studies, the shock-wave modulation induced by turbulence should be investigated to accurately predict sonic booms. To develop a tool for sonic boom prediction, it can be considered that local and instantaneous pressure waveform should be predicted. However, it is difficult to investigate the interaction between a shock wave and atmospheric turbulence because of the complexities of atmospheric turbulence, such as mean velocity and density profile. In addition, it is also difficult to

guarantee reproducibility of local and instantaneous properties of shock wave modulation induced by turbulence. Therefore, statistical investigations are necessary for the shock wave modulation at first. In this thesis, the statistical properties of pressure jump fluctuations of a normal shock wave and shock-wave deformation induced by HIT are investigated. In addition, intermittency of atmospheric turbulence has been investigated [35]. It can be considered that shock waves propagating in the atmosphere repeat the incident process to a turbulent region, interaction with the turbulence, and escape process from the turbulent region. This is why the transient process of the shock wave modulation is important for the sonic boom prediction and the effects of interaction length are investigated in Chapter 3. These studies involve using DNSs of interactions between a normal shock wave and HIT. Shock-wave and turbulence conditions are controlled so that the results can be compared with previous experimental results. In addition, statistical characteristics of shock-wave deformation and the effects of interaction length on shock-wave deformation are examined against the DNSs of a normal shock wave propagating in a local turbulent region.

Statistical investigations on the pressure jump fluctuations across a normal shock wave are performed in Chapter 2. DNSs of a normal shock wave interacting with HIT with a turbulent Mach number much lower than previous studies because of the low turbulent Mach number of atmoshperic turbulence, and pressure jump fluctuations in the shock wave induced by HIT are investigated. At first, the local pressure jump is defined in the case of a normal shock wave interacting with HIT, and the relations between rms values of the fluctuations of the pressure jumps and $M_t/(M_s-1)$ or $M_t^2/(M_s^2-1)$ are confirmed. Then, some of the statistics of the fluctuations of the pressure jumps and the correlation coefficient between the fluctuations of the pressure jumps and velocity fluctuations of turbulence are calculated. Any relationship between the local shock-wave deformation and local velocity shear are investigated.

In Chapter 3, the statistical properties of shock-wave deformation are investigated. The results of effects of interaction length on the shock-wave deformation is one of the most important results of this thesis. The results imply importance of the interaction

length for shock-wave deformation. Here, shock-wave deformation is defined from the local shock-wave position detected by the minimum values of pressure gradients in the direction of the shock-wave propagation. Although shock-wave deformation has been studied via both experiments and numerical simulations, few data can be compared. Therefore, shadowgraph visualizations from numerical data are also performed. The relations between shock-wave deformation and local shock strength are then investigated. In Chapter 3, some of the statistics are plotted against $M_t/(M_s - 1)$ or $M_t^2/(M_s^2 - 1)$, introduced for parameters in the shock–turbulence interaction [11], [15], [26], [27].

Statistical properties of the pressure jump fluctuations in the shock wave and shock-wave deformation are investigated in this study. The pressure jump fluctuations are induced by the velocity fluctuations normal to the shock wave in turbulence. In addition, the local propagation direction of the shock wave is related to velocity shear in turbulence. This result supports the model introduced by Inokuma et al. [30]. In addition, shock-wave deformation is statistically investigated, and the effects of the interaction length are revealed. From the result, it is implied that the transient process of the shock wave modulations is important in shock–turbulence interaction. These statistical results are the first steps for the development of a tool for sonic boom prediction.

Chapter 2

Fluctuations of pressure jumps across a normal shock wave caused by an interaction with homogeneous isotropic turbulence

2.1 Introduction

Changes in shock-wave properties due to interaction with turbulence are less understood compared with the shock-wave influences on turbulence. The fluctuations of pressure jumps across the shock wave have hardly been discussed, even with recent high-resolution DNSs of shock–turbulence interactions. One of the important findings in recent experimental studies is the finite response time in the modulation of the pressure jump across the shock wave due to interactions with turbulence [30]. This indicates that the shock-wave properties possess strong memories and exhibit non-locality in time. Inokuma *et al.* gave a possible explanation for this feature of shock–turbulence interactions based on a timescale of shock-wave deformation due to a fluid-velocity perturbation [30].

In this chapter, DNSs of interactions between a normal shock wave and homogeneous isotropic turbulence with a turbulent Mach number much lower than previous numerical studies are performed. The low turbulent Mach number is similar to the turbulent Mach number of atmospheric turbulence, which plays an important role in the sonic boom problem. Therefore, the motivation of this study is investigating pressure jump fluctuations in the shock wave induced by such turbulence with a low turbulent Mach number. Statistical properties of the pressure jump fluctuations and relationships between the pressure jump fluctuations and velocity fluctuations are investigated via these DNSs. In addition, relationships between local propagation directions of the shock wave and velocity shear of turbulence are investigated. These DNSs results in this chapter support existing experimental findings regarding the finite response time in shock-wave modulations induced by turbulence interactions, though the present DNSs cover a higher shock Mach number range than the previous experiment that demonstrated finite response time [30].

2.2 Direct numerical simulations

2.2.1 Flow field and parameters of the shock wave and turbulence

In these DNSs, a normal shock wave interacts with HIT without a mean flow; the schematic view is shown in Figure 2.1. The cubic computational domain with a side length of 0.06 [m] is represented by $N^3 = 384^3$ or 512^3 grid points. The direction of the shock-wave propagation is denoted by x, while y and z represent the shock-tangential directions. The normal shock wave is inserted from the y-z plane at $x = 0$ [m], which is the boundary of the computational domain, by substituting the physical quantities calculated from the mean characteristics of the HIT and a shock Mach number with Rankine-Hugoniot relations. Hereafter, the time when the shock wave is inserted in the computational domain is set to $t = 0$. Following insertion, the shock wave propagates through the computational domain in the x direction with time advancement until it

reaches the boundary at $x = 0.06$ [m].

The parameters of the shock wave and turbulence are summarized in Table 2.1. It is expected that the effects of turbulence on the shock wave increase with a weaker shock wave for a fixed turbulent Mach number [27]. Furthermore, LIA predicts that an interaction between a weak shock wave and turbulence depends on shock Mach number, such as when $M_s < 1.5$ [12]. For these reasons, DNSs with the shock Mach numbers $M_s = 1.1, 1.3$ and 1.5 are performed, denoted by Cases 2-1, 2-2, and 2-3, respectively. The DNS results of Case 2-3 are compared for different numbers of grid points, 384^3 and 512^3, so that grid convergence may be analyzed in the next section. DNSs of the other cases are performed with 384^3 grid points. The shock waves with these shock Mach numbers interact with the same turbulence. Additional simulations are performed using the HIT developed from two independent initial conditions generated from different sets of random numbers. The HIT has a turbulent Mach number of $M_t = 2.96 \times 10^{-4}$ and turbulent Reynolds number of $Re_\lambda \equiv u'_{rms}\lambda/\langle\nu\rangle \approx 18$, where $u'_{rms} = 0.102$ [m/s] is the rms value of velocity flutuations, $\lambda \equiv u'_{rms}/(\partial u/\partial x)'_{rms} = 2.70 \times 10^{-3}$ [m] is the Taylor microscale, $\langle\nu\rangle = 1.53 \times 10^{-5}$[m^2/s] is the mean kinematic viscosity, and $\langle a\rangle = 342$ [m/s]

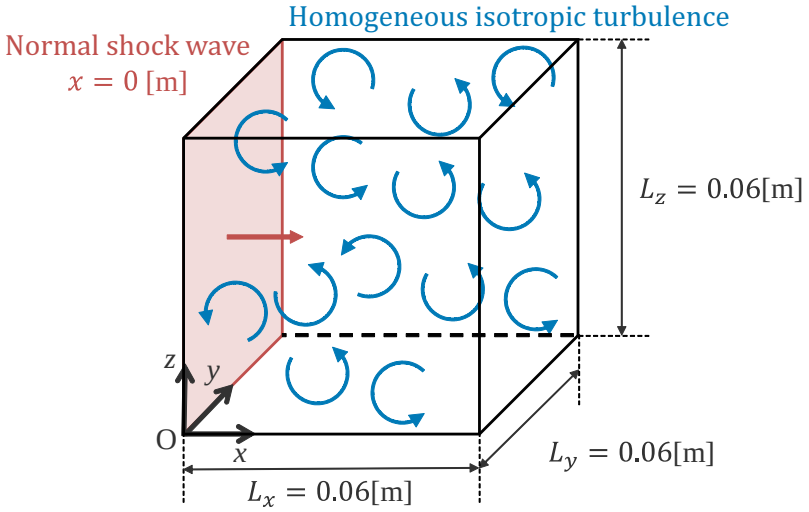

Figure 2.1. Schematic view of the DNSs of a normal shock wave interacting with homogeneous isotropic turbulence.

is the mean speed of sound. Mean pressure, density, and temperature are $\langle p \rangle = 101496$ [Pa], $\langle \rho \rangle = 1.21$ [kg/m^3], and $\langle T \rangle = 293$ [K], respectively. These statistical values of the HIT are calculated from volume averages taken in the whole computational domain, denoted as $\langle * \rangle$. Table 2.1 summarizes the parameters of the spherical shock wave and grid turbulence [30].

The initial HIT is generated according to Ref. [36] by prescribing an energy spectrum of $E(k) \sim k^4 \exp[-2(k/k_0)^2]$, where k is the wavenumber and $E(k)$ peaks at $k = k_0$ ($1/k_0 = 1.7 \times 10^{-3}$ [m]). The turbulence is temporally advanced until three eddy turnover times ($= L/u'_{rms}$: L is the integral length scale) in a periodic cube. The longitudinal integral length scale $L \equiv \int_0^\infty f(r)dr$ is calculated from a longitudinal auto-correlation function $f(r)$. The Kolmogorov length scale $\eta \equiv (\langle \nu \rangle^3 \langle \rho \rangle / \langle \varepsilon \rangle)^{1/4}$ of the HIT are $L = 4.61 \times 10^{-3}$ [m] and $\eta = 3.19 \times 10^{-4}$[m], respectively, where $\varepsilon \equiv \tau_{ij} S_{ij}$ is the dissipation rate of turbulent kinetic energy. Here, τ_{ij} is the shear stress tensor, and $S_{ij} \equiv (\partial u_i/\partial x_j + \partial u_j/\partial x_i)/2$ is the rate-of-strain tensor. The side length of the computational domain is about $13L$, and the grid spacing is $\Delta = 0.49\eta$ for 384^3 grid points and $\Delta = 0.37\eta$ for 512^3 grid points. These grid spacings are small enough to consider small-scale fluctuations in the HIT [37]. Although physical quantities discontinuously change across the shock waves in real situations, the discontinuous jumps are treated with few grid points in DNSs to suppress spurious numerical oscillations. A very high resolution is required to prevent spatial resolution from affecting the shock-wave characteristics. Therefore, the spatial resolution in the present DNS is very high in terms of the Kolmogorov length scale. Figure 2.2 shows skewness at $S \equiv \langle (\partial u'/\partial x)^3 \rangle / (\partial u'/\partial x)^3_{rms}$ and flatness at $F \equiv \langle (\partial u'/\partial x)^4 \rangle / (\partial u'/\partial x)^4_{rms}$ of the longitudinal velocity derivative $\partial u'/\partial x$ as functions of Re_λ. The results are in good agreement with previous studies [38]–[46], confirming that the turbulence is developed enough to possess the well-known characteristics of turbulence at the present value of Re_λ. In addition, the Kolmogorov time scale $t_\eta \equiv (\langle \nu \rangle / \langle \varepsilon \rangle)^{1/2} = 6.65 \times 10^{-3}$[s], the smallest HIT time scale, is much larger than the time during which the shock wave moves from $x = 0$[m] to $x = 0.06$[m], even in the longest case of Case 2-1 (1.59×10^{-4}s). This demonstrates that the HIT is almost stationary

Table 2.1. Parameters of the shock wave and turbulence compared with experiments of interaction between a spherical shock wave and grid turbulence [30].

Case	M_s	Re_λ	M_t	u'_{rms} [m/s]	L [mm]
2-1	1.1	18	2.96×10^{-4}	0.102	4.61
2-2	1.3	18	2.96×10^{-4}	0.102	4.61
2-3 ($N = 384$)	1.5	18	2.96×10^{-4}	0.102	4.61
2-3 ($N = 512$)	1.5	18	2.96×10^{-4}	0.102	4.61
Ref.1 [30]	1.004	102	1.1×10^{-3}	0.387	27.5
Ref.2 [30]	1.004	200	2.3×10^{-3}	0.798	48.1
Ref.3 [30]	1.004	149	1.6×10^{-3}	0.568	54.3
Ref.4 [30]	1.004	296	3.4×10^{-3}	1.17	64.3

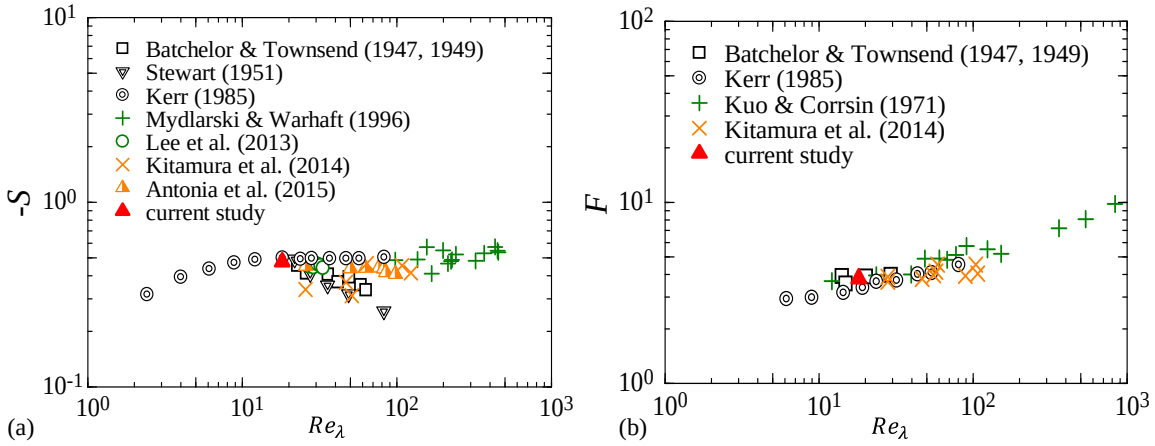

Figure 2.2. (a) Skewness and (b) flatness of longitudinal velocity gradient as functions of turbulent Reynolds number compared with previous studies using a wide range of turbulent Reynolds numbers.

during the propagation process of the shock wave in all cases.

2.2.2 Governing equations and numerical schemes

The three-dimensional, compressible Navier-Stokes equations are solved for simulations of shock–turbulence interaction as follows:

$$\frac{\partial \rho}{\partial t} + \frac{\partial \rho u_j}{\partial x_j} = 0, \tag{2.1}$$

$$\frac{\partial \rho u_i}{\partial t} + \frac{\partial (\rho u_i u_j + \delta_{ij} p)}{\partial x_j} = \frac{\partial \tau_{ij}}{\partial x_j}, \tag{2.2}$$

$$\frac{\partial e}{\partial t} + \frac{\partial (e+p) u_j}{\partial x_j} = \frac{\partial \tau_{ij} u_i}{\partial x_j} + \frac{\partial}{\partial x_j}\left(\kappa \frac{\partial T}{\partial x_j}\right), \tag{2.3}$$

with a constant specific heat ratio of $\gamma = 1.4$ and the equation of state for a perfect gas as follows:

$$p = \rho R T. \tag{2.4}$$

Here, t is the time, x_i is the position in i direction, ρ is the density, u_i is the velocity component in i direction, $e = P/(\gamma - 1) + \rho u_j^2/2$ is the total energy, p is the pressure, T is the temperature, $R = 287$ [J/(kg K)] is the gas constant, κ is the thermal conductivity, and δ_{ij} is the Kronecker delta. The shear stress tensor τ_{ij} is represented using the Stokes hypothesis as follows:

$$\tau_{ij} = \mu \left(\frac{\partial u_i}{\partial x_j} + \frac{\partial u_j}{\partial x_i} - \frac{2}{3} \delta_{ij} \frac{\partial u_k}{\partial x_k} \right), \tag{2.5}$$

where μ is the viscosity coefficient calculated by Sutherland's law.

The DNS code is based on the finite-volume method with the fourth-order Runge-Kutta time advancement and hybrid Roe flux splitting with weighted essentially non-oscillatory (WENO)/central difference scheme. The Roe flux splitting with the fifth-order WENO scheme is applied to a near shock region, which suppresses numerical oscillation caused by the discontinuity in the shock wave, whereas the sixth-order central difference scheme is used in the region far from the shock wave [26]. Numerical dissipation allows the Roe flux splitting to attenuate small-scale turbulence fluctuations. This is why the hybrid scheme is used here. The shock wave is detected with a sensor defined as $\phi = (\nabla \cdot \mathbf{u})^2 / [(\nabla \cdot \mathbf{u})^2 + (\nabla \times \mathbf{u})^2 + \varepsilon_\phi]$ [47], where $\mathbf{u}$ is the velocity vector and $\varepsilon_\phi = 10^{-16}$ [$1/\mathrm{s}^2$] is a constant to prevent the denominator from being zero (thus, $0 \leq \phi < 1$). ϕ is close to 1 near the shock wave due to strong compression, while $\phi \ll 1$ in the region far from the shock wave because the turbulence is almost incompressible in the present

DNSs. Roe flux splitting is applied for the region with $\phi > 10^{-2}$, and the central difference scheme is applied in the other region. Special treatments are not used in the interface between the WENO and the central difference schemes because the difference in density across the interface is very small due to the low turbulent Mach number. Owing to the threshold for ϕ, Roe flux splitting is applied only in the region near the shock wave, and numerical oscillations are not observed near the interface between the WENO and the central difference schemes. The present code is auto-parallelized by a FORTRAN compiler on a high-performance computing system (NEC SX-9: a vector supercomputer) because the program can be run with large shared memory. The present code has been validated in simulations of a laminar boundary layer, a shock tube problem, and a shock–vortex interaction, the results of which agree well with analytical solutions [48], [49].

The boundary condition at $x = 0$ determines the mean flow state behind the shock wave. During shock wave propagation, the boundary at $x = 0$ [m] (behind the shock wave) is treated with the Dirichlet boundary condition. The physical quantities behind the shock wave are used to insert the shock wave. Conversely, the zero-gradient condition is applied to the boundary at $x = 0.06$ [m]. The periodic boundary conditions are used in y and z directions.

2.3 Results and discussion

2.3.1 Shock-wave propagation in homogeneous isotropic turbulence

The shock wave and vortex structures are visualized in Figure 2.3(a) with a large negative value of dilatation ($\theta < 0$) and a positive value of the second invariants of the velocity gradient tensor ($Q > 0$), respectively. Here, dilatation is calculated by $\theta \equiv \nabla \cdot \mathbf{u}$, and the second invariants are calculated by $Q \equiv (W_{ij}W_{ij} + \theta^2 - S_{ij}S_{ij})/2$, where $W_{ij} \equiv (\partial u_i/\partial x_j - \partial u_j/\partial x_i)/2$ is the rate-of-rotation tensor. The visualization demonstrates that strong shock-wave compression squeezes the vortex structures, sim-

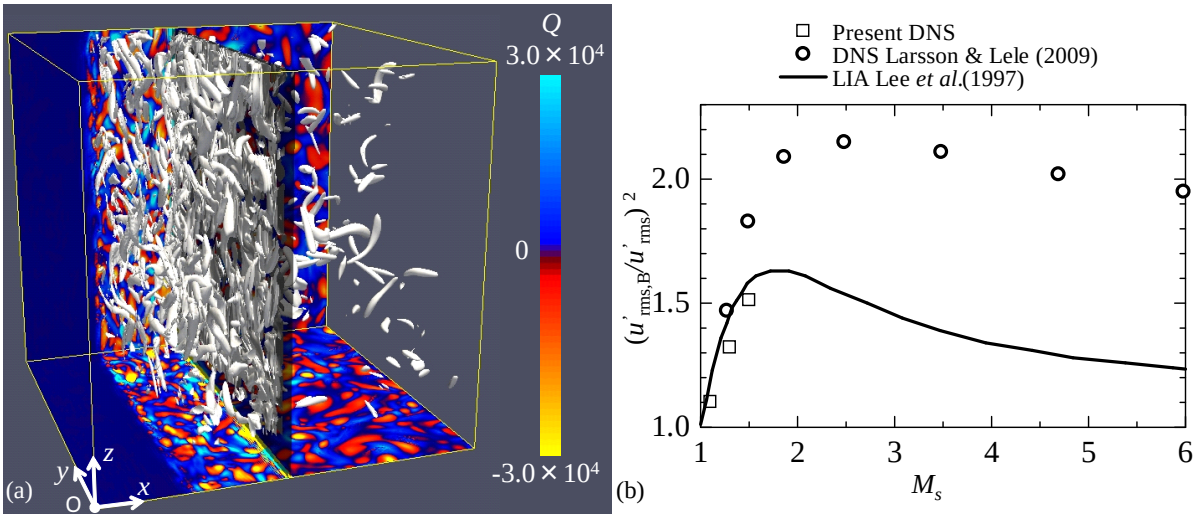

Figure 2.3. (a) Visualizations of the shock wave and turbulent vortex structures visualized by the isosurfaces of a large negative value of dilatation θ (gray) and a positive value of the second invariants of the velocity gradient tensor Q (white), respectively. The x-y plane at $z = 0$ [m] and x-z plane at $y = 0.06$ [m] are colored by Q with $M_s = 1.5$ (Case 2-3). (b) Amplification rate of the rms value of the velocity fluctuations in x direction by the shock wave. The present DNS results are compared with a previous DNS [26] and LIA [12].

ilar to that observed in a previous study [27]. The shock wave induces a mean flow behind the propagating shock wave [50], and there is a laminar flow region between the boundary at $x = 0$ [m] and the end of the turbulent region. The laminar flow region is not treated in the following statistical analysis. Figure 2.3(b) shows an amplification rate of the rms values of the velocity fluctuations in the x direction, $(u'_{rms,B}/u'_{rms})^2$, where $u'_{rms,B} \equiv \sqrt{\langle (u'_B)^2 \rangle}$ is the rms value of the velocity fluctuations in the x direction in the turbulent region behind the shock wave, u'_B, and u'_{rms} is the rms value of velocity fluctuations of the HIT before the interaction. The M_s dependence of the amplification rate $(u'_{rms,B}/u'_{rms})^2$ agrees well with a previous DNS study [26] and LIA [12]. This confirms that the present DNS code can adequately simulate the shock–turbulence interaction.

The shock-wave position x_s is plotted as functions of time in Figure 2.4. The x_s can be obtained as a position where the mean dilatation $\overline{\theta}(x;t)$ is the smallest. Here, $\overline{\theta}(x;t)$ is obtained by averaging in homogeneous y and z directions. The shock-wave

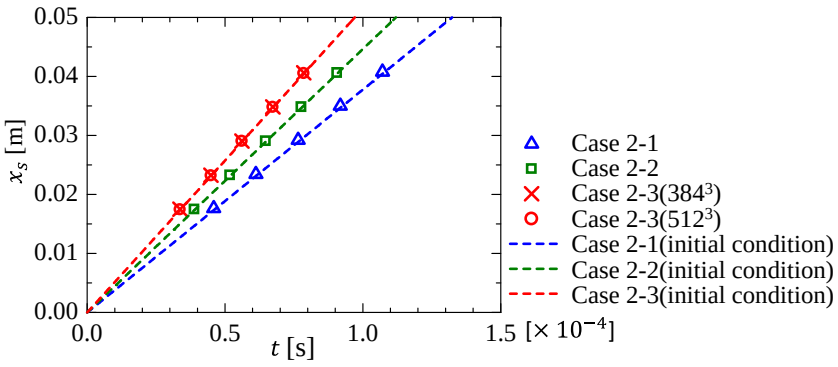

Figure 2.4. The shock-wave position (x_s) as a function of t, where the shock wave is inserted in a domain at $t = 0$. Symbols (blue triangles, green squares, and red crosses and circles) are x_s at different time steps, which are obtained from positions where the mean dilatation profile $\overline{\theta}(x;t)$ is the smallest. Lines denote the prediction that $x_s = M_s\langle a\rangle t$ with the initial values of M_s.

position calculated as $x_s = M_s\langle a\rangle t$ is also shown as straight lines in Figure 2.4, where M_s is the initial shock Mach number. Pressure waves generated by turbulent motion can be reflected when the waves reach the boundaries at $x = 0$ [m] and $x = 0.06$ [m] because the boundary conditions are not non-reflective. The spurious reflected pressure waves can affect the shock wave and change its propagation velocity. As shown in Figure 2.4, the shock-wave positions detected in the DNSs agree well with the estimation of $x_s = M_s\langle a\rangle t$, confirming that the propagation process does not affect the shock wave's propagation velocity. One of the reasons for the boundary condition's negligible influence is the very low turbulent Mach number. Furthermore, the velocity of shock-wave propagation for $M_s = 1.5$ does not depend on the number of grid points.

2.3.2 Pressure jumps across the shock wave

In this section, pressure jumps across the shock wave are defined and analyzed, and their relationship to velocity fluctuations is discussed. The local pressure jump across the shock wave is defined as follows: first, a non-dimensional mean pressure jump Δp_r is calculated as

$$\Delta p_r(x;t) \equiv \frac{\overline{p}(x;t) - p_F}{p_B - p_F}, \tag{2.6}$$

where $\overline{p}(x;t)$ is the plane average taken in the homogeneous y and z directions, p_F is the pressure in front of the shock wave, and p_B is the pressure behind the shock wave per the Rankine-Hugoniot relation to p_F. The position of x_p is then determined where the local pressure jump is evaluated. x_p is chosen as the position at which Δp_r becomes larger than the threshold p_{th} across the shock wave from the front. The threshold p_{th} is defined by $1 - p_{th} = 10^{-4}$ because the results stay largely the same across the range of $10^{-6} \leq 1 - p_{th} \leq 10^{-3}$. x_p is defined based on the mean pressure profile because the low turbulent Mach number allows the shock wave to keep its initial flat shape, even during the interaction [27]. Finally, the local pressure jump across the shock wave can be calculated as $\Delta p(y,z;t) \equiv p(x_p,y,z;t) - p_F$. The average of Δp on a y-z plane denoted by $\overline{\Delta p}$ is obtained as a function of t. The fluctuations of Δp are calculated as $\Delta p'(y,z;t) \equiv \Delta p(y,z;t) - \overline{\Delta p}(t)$. Figure 2.5 shows the two-dimensional profiles of $\Delta p'/\Delta p'_{rms}$ when the shock wave is at the center of the computatinoal domain ($x \approx 0.03$ [m]), where $\Delta p'_{rms}$ is the rms value of $\Delta p'$. Here, y and z are normalized by the integral length scale of turbulence L. The turbulence change induces fluctuations of Δp as M_s increases. The characteristic length scale of the fluctuations increases with lower M_s. Furthermore, $\Delta p'$ exhibits a very similar profile for Cases 2-2 and 2-3. The effects of grid spacing on the pressure jump fluctuations are described in the Appendix.

The values of $\Delta p'_{rms}(t)$ are calculated in several snapshots, each of which has the shock wave in a different position. $\Delta p'_{rms}(t)$ is plotted against $x_p(t)$ in Figure 2.6. $\Delta p'_{rms}(t)$ is calculated after the shock wave propagates more than thrice the integral length scale. In Case 2-1, $\Delta p'_{rms}$ increases until the shock wave reaches $x_p \approx 5.9L$ but becomes almost stationary state when $x_p > 5.9L$. This indicates that $\Delta p'_{rms}$ increases from the initial condition without fluctuations ($\Delta p'_{rms} = 0$) until the fluctuations reach a statistically stationary state with an almost constant $\Delta p'_{rms}$. The following analyses use the data from after the shock wave reaches an almost statistically stationary state ($x_p > 5.9L$). $\Delta p'_{rms}$ is smaller in Case 2-1 than in the other two cases. There is no observable dependence on the shock Mach number for $M_s \geq 1.3$, as shown in the visualizations in Figure 2.5.

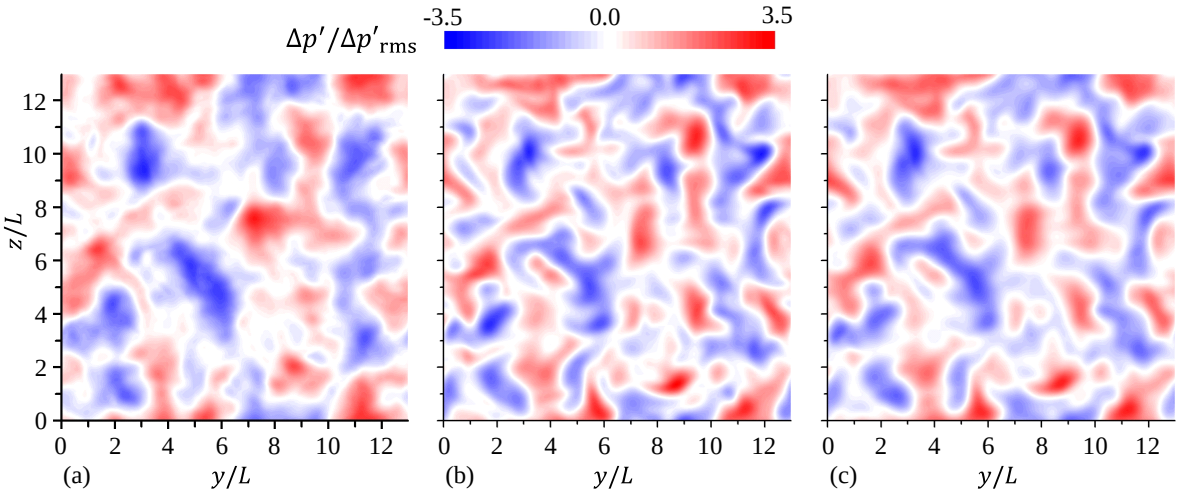

Figure 2.5. Profiles of the fluctuations of normalized pressure jumps, $\Delta p'/\Delta p'_{rms}$, on the y-z plane at $x = x_p$: (a) Case 2-1, (b) Case 2-2, and (c) Case 2-3 with 384^3.

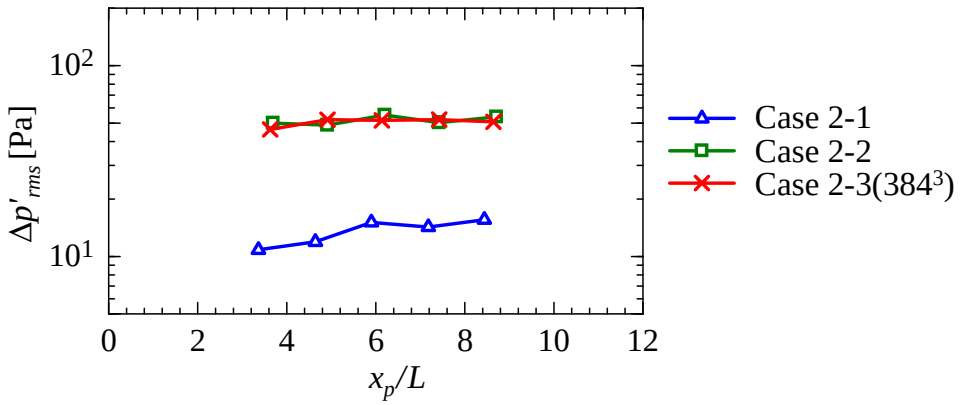

Figure 2.6. $\Delta p'_{rms}(t)$ plotted as functions of $x_p(t)$.

Figure 2.7(a) shows pressure fluctuations p' in the initial HIT on the y-z plane at the center of the computational domain ($x = 0.03$ [m]). The rms value of the HIT pressure fluctuations is of the order of 10^{-2} Pa, which is much smaller than $\Delta p'_{rms}$. Conversely, Figure 2.7(b) shows p' normalized by its rms value p'_{rms}. The figure also visualizes small spots with large and negative values of p'/p'_{rms}; these spots are related to a vortex core with $Q \gg 0$, which appears around local minimum values of p' because of the relation of $2Q = \nabla^2(p/\rho)$ in conditions of low M_t turbulence [51].

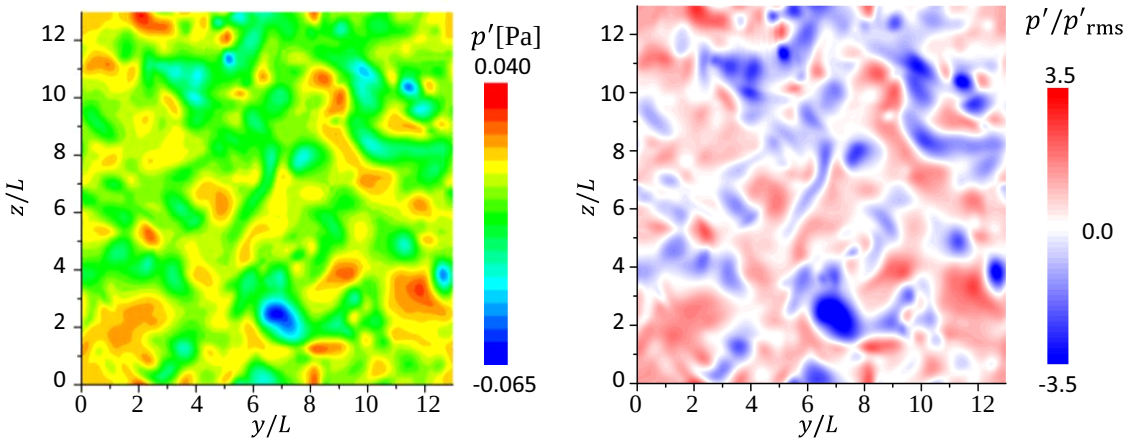

Figure 2.7. Pressure fluctuations in the initial HIT on the y-z plane ($x = 0.03$ [m]) in (a) Pa and (b) nondimensional form.

Table 2.2. Summary of DNS results compared with the experiments [30].

Case	$\Delta p'_{rms}$ [Pa]	$\Delta p'_{rms}/\overline{\Delta p}$	$\Delta x_P/L$	δ_s [mm]
2-1	14.9	0.60×10^{-3}	-0.64	1.1
2-2	52.6	0.63×10^{-3}	-1.1	0.67
2-3 ($N = 384$)	51.5	0.35×10^{-3}	-0.40	0.60
2-3 ($N = 512$)	57.7	0.39×10^{-3}	-0.58	0.43
Ref.1 [30]	38.4	2.69×10^{-2}	-4.8	–
Ref.2 [30]	72.1	6.20×10^{-2}	-2.9	–
Ref.3 [30]	46.8	3.38×10^{-2}	-3.5	–
Ref.4 [30]	102.2	7.03×10^{-2}	-1.9	–

Table 2.2 summarizes the DNS results compared with the experimental results of interactions between a spherical shock wave and grid turbulence [30]. The orders of $\Delta p'_{rms}$ in these DNSs are the same as the ones obtained in the experiments, although the shock Mach numbers of the present DNSs are much larger ($M_s = 1.004$). $\Delta p'_{rms}/\overline{\Delta p}$, which represents the relative intensity of the pressure jump fluctuations, significantly depends on the shock Mach number M_s, where $\Delta p'_{rms}/\overline{\Delta p}$ tends to shrink as M_s increases.

It is expected that Δp_r in Equation (2.6) will change from 0 to 1 across the shock

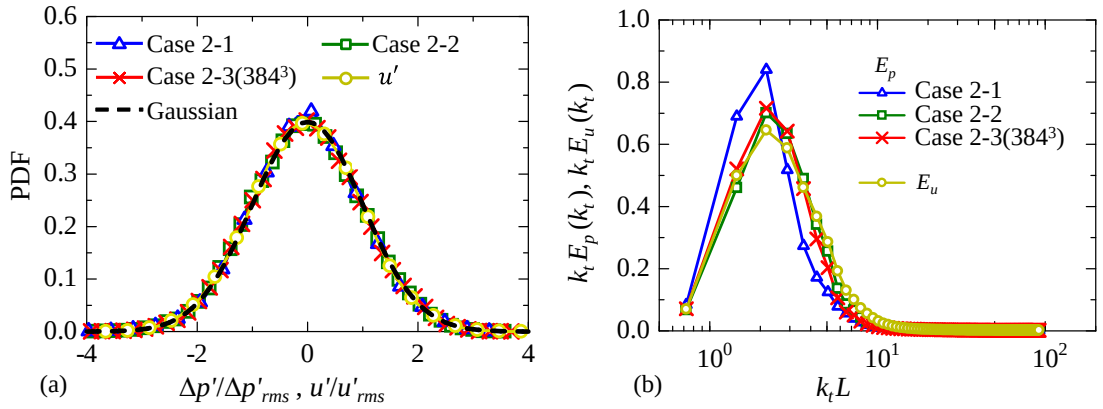

Figure 2.8. (a) PDFs of the fluctuations of normalized pressure jumps, $\Delta p'/\Delta p'_{rms}$, across the shock wave and normalized velocity fluctuations u'/u'_{rms} of the HIT. (b) Energy spectra of $\Delta p'/\Delta p'_{rms}$ and u'/u'_{rms} in an area-preserving form. k_t is the wavenumber tangential to the shock wave. The spectrum of u'/u'_{rms} is computed from the HIT.

wave. Therefore, $\Delta p_r(x)$ can be approximated as follows:

$$\Delta p_r = \frac{1}{2} + \frac{1}{2}\tanh\left(\frac{x - x_s}{\delta_s/4}\right). \tag{2.7}$$

Here, the thickness of the shock wave, δ_s, is estimated using the least squares method, summarized in Table 2.2. The factor of $1/4$ is added so that δ_s represents the distance between two points where Δp_r increases from 0 and 1. In these DNSs, δ_s is much larger than the mean free path of about 6.8×10^{-8} [m] in the atmosphere, and it is of the order of the Kolmogorov length scale for the HIT because the shock waves in these DNSs are treated with a Roe flux splitting.

Figure 2.8(a) shows the probability density functions (PDFs) of $\Delta p'$ normalized by $\Delta p'_{rms}$, together with the Gaussian profile and the PDF of velocity fluctuations before the interaction of u' in the HIT. The PDFs of $\Delta p'$ and u' are well approximated by the Gaussian profile, in agreement with previous experimental studies of shock–turbulence interaction [29]. The energy spectra of $\Delta p'/\Delta p'_{rms}$ and u'/u'_{rms} (denoted by E_p and E_u, respectively) are computed based on the one-dimensional Fourier transform in the y (z) direction, where k_t is the wavenumber tangential to the shock wave. Figure 2.8(b) shows E_p against $k_t L$ in an area-preserving form with E_u in the HIT. The spatial distribution

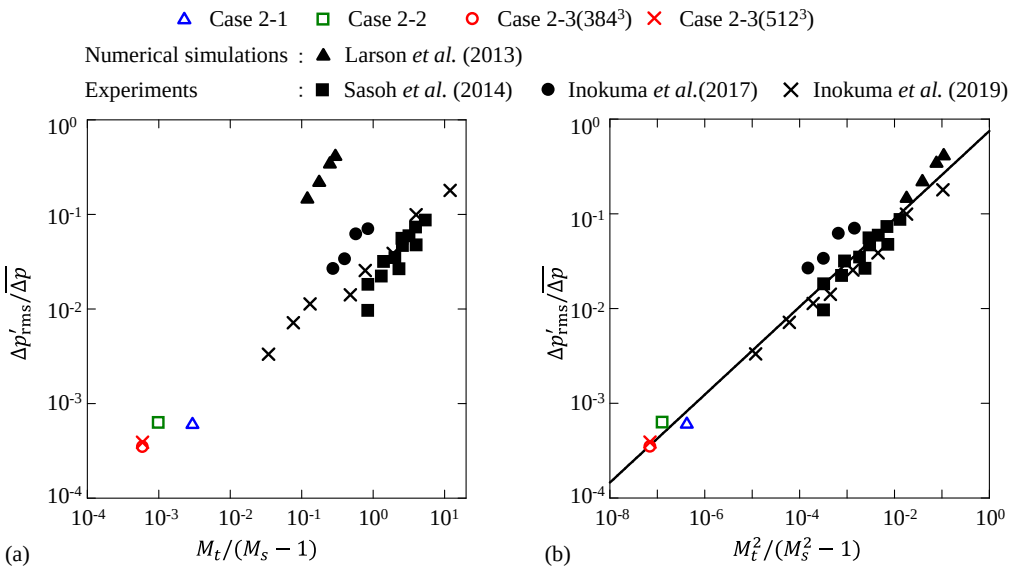

Figure 2.9. Relative intensity of pressure jump fluctuations $\Delta p'_{rms}/\overline{\Delta p}$ plotted against (a) $M_t/(M_s-1)$ and (b) $M_t^2/(M_s^2-1)$. The straight line in (b) represents $\Delta p'_{rms}/\overline{\Delta p} \sim (M_t^2/(M_s^2-1))^{0.46}$ obtained using the least squares method. DNS results are compared with those of previous experiments [29]–[31] and numerical simulations [27].

of $\Delta p'$ is characterized by a large scale, as attested by the peaks around $k_t L = 2$. E_p's peak wavenumber is consistent with that of E_u. Further, more energy is contained in larger scales in Case 2-1 despite the shock waves interacting with the same turbulence in all cases.

Larsson *et al.* demonstrated that shock wave geometry during turbulence interaction is characterized by $M_t/(M_s-1)$ [27]. Inokuma *et al.* assert that the pressure jump fluctuations across a shock wave are characterized by $M_t^2/(M_s^2-1)$ [31]. Figures 2.9(a) and (b) show the relative intensity of the fluctuations of the pressure jumps $\Delta p'_{rms}/\overline{\Delta p}$ plotted against $M_t/(M_s-1)$ and $M_t^2/(M_s^2-1)$, respectively. These figures include the data of previous experiments [29]–[31] and numerical simulations [27]. The values of $\Delta p'_{rms}/\overline{\Delta p}$ from the numerical simulations performed by Larsson *et al.* [27] are calculated using the method proposed by Inokuma *et al* [31]. Figures 2.9(a) and (b) show that $\Delta p'_{rms}/\overline{\Delta p}$ is better characterized by $M_t^2/(M_s^2-1)$ than $M_t/(M_s-1)$, as reported by Inokuma *et al.* [31]. The least squares method for all data points yields $\Delta p'_{rms}/\overline{\Delta p} \sim$

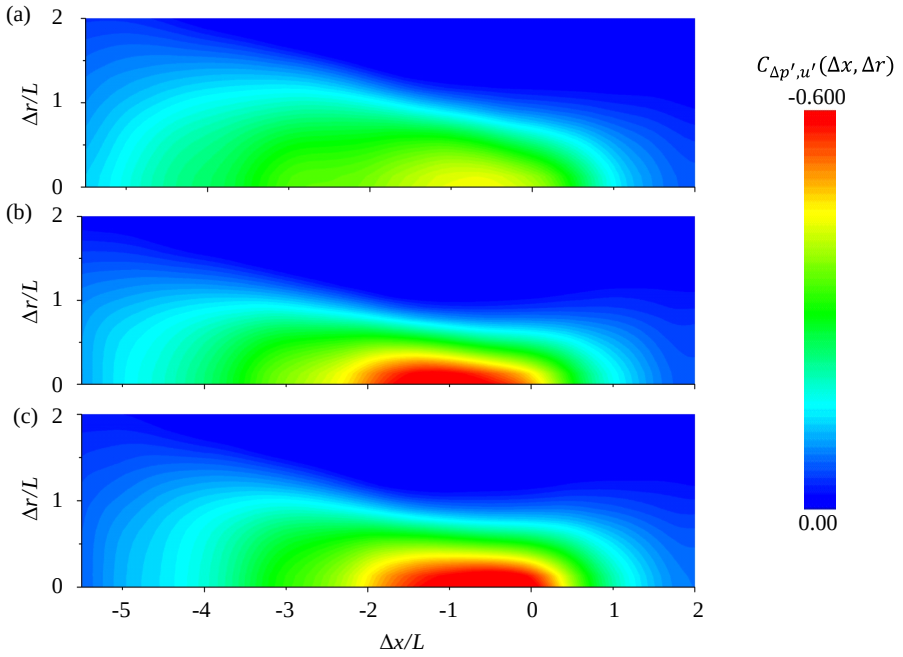

Figure 2.10. Two-point correlation coefficients $C_{\Delta p',u'}(\Delta x, \Delta r)$ between the fluctuations of the pressure jumps across the shock wave, $\Delta p'(y,z;t)$ evaluated at $x_p(t)$, and the velocity fluctuations in the x direction of the initial HIT, $u'(\mathbf{x_p}+\mathbf{\Delta};t=0)$, where $\mathbf{x_p}=(x_p,y,z)$: (a) Case 2-1, (b) Case 2-2, and (c) Case 2-3 with 384^3 grid points. The separation vector $\mathbf{\Delta}$ is decomposed into the normal (Δx) and tangential (Δr) distances.

$[M_t^2/(M_s^2-1)]^{0.46}$.

2.3.3 Two-point correlation between pressure jumps and turbulent velocity fluctuations

To calculate the two-point correlation coefficient $C_{\Delta p',u'}$ between $\Delta p'(y,z;t)$ at $x_p(t)$ and $u'(\mathbf{x_p}+\mathbf{\Delta};t=0)$, $\mathbf{x_p}=(x_p,y,z)$ and $\mathbf{\Delta}$ is the separation vector. Here, an average of $C_{\Delta p',u'}$ is taken for all points in the y-z plane. $u'(x,y,z)$ at $t=0$ is used because the turbulence is frozen in the propagation process of the shock wave due to the low turbulent Mach number. To obtain converged statistics, an ensemble average of $C_{\Delta p',u'}$ is calculated using six snapshots in the stationary state of $x_p \geq 5.9L$ in two DNS realizations.

Figure 2.10 illustrates $C_{\Delta p',u'}$ for all cases, where the separation vector $\mathbf{\Delta}$ decomposes

into the normal and tangential directions of the shock wave represented by $\Delta x = \boldsymbol{\Delta} \cdot \mathbf{e}_x$ and $\Delta r = |\boldsymbol{\Delta} - \Delta x \mathbf{e}_x|$ ($\mathbf{e}_x$: the unit vector in the x direction). The resultant correlation is negative; thus, the pressure jumps are amplified in the case where the shock wave interacts with the velocity fluctuations opposed to the direction of shock-wave propagation, creating a negative u', and vice versa. The strong correlation appears in the region $-2 \leq \Delta x/L \leq 0$ and $0 \leq \Delta r/L \leq 0.5$. Thus, the velocity fluctuations located in the region dominantly influences the fluctuations of the pressure jumps. In addition, The negative correlation peaks behind the shock wave at $\Delta r = 0$, with the distance denoted by Δx_P, as shown in Table 2.2. $|\Delta x_P|$ is close to the integral length scale L, although the exact values of $\Delta x_P/L$ vary depending on the conditions. These results are consistent with previous experimental results and hardly depend on spatial resolution, as shown in the Appendix. The distance between the shock wave and the peak correlation behind it suggests that the turbulence in the region where the shock wave has already passed has a stronger influence on $\Delta p'$ than the region where the shock wave is currently. Simply put, turbulence has the most influence after the shock wave propagates across $\sim L$. $\Delta p'$ evaluated at a given shock wave ray is strongly affected by turbulence on the same ray, as shown by the strong correlation around $\Delta r \approx 0$. It should be noted that the correlation coefficient does not monotonically increase with the shock Mach number. Similar results concerning the correlation coefficient were reported in experiments on the interaction between a spherical shock wave and grid turbulence [30]. $C_{\Delta p',u'}$ has a negative value even for $\Delta r \approx L$. This can be related to a large-scale vortex in which $\sim L$ contains a large part of the turbulent kinetic energy. In Case 2-1, the negative correlation exhibited a larger Δr than the other two cases. This indicates that pressure jumps can be affected by velocity fluctuations far away from the shock ray of a weak shock wave. These velocity fluctuations can weaken the shock ray correlation because the pressure jumps across the shock wave are affected by turbulence not only on the shock ray but also far from it. Finally, $\Delta p'$ does not not correlate with the other quantities, such as fluid velocity in the shock-tangential directions (v and w), pressure fluctuations in HIT, and enstrophy. This implies that the fluctuations pressure jumps

across the shock wave are induced by velocity moving in a shock-normal direction in front of the shock wave.

2.3.4 Shock wave deformation model for turbulent effects on a shock wave

Inokuma *et al.* [30] proposed a physical model to explain the effects of turbulence on a pressure jump across a shock wave based on shock-wave deformation induced by turbulence velocity fluctuations. The conceptual picture of this model is shown in Figure 2.11. The picuture is drawn two-dimensionally although their model is three dimensional. The setup considered in the model is a normal shock wave interacting with a fluid with a velocity fluctuation normal to the shock wave varying in the shock-tangential direction. The propagation velocity of the shock wave is defined as the relative velocity of the shock wave's moving velocity to fluid velocity at the shock-

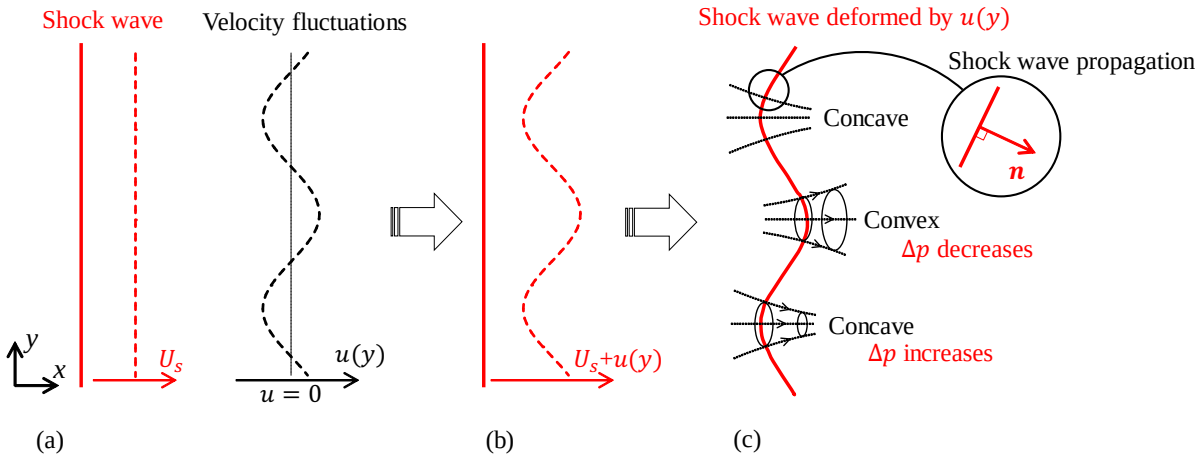

Figure 2.11. A shock-wave-deformation model of turbulent effects on a shock wave. The red solid line represents a shock wave, while black and broken red lines represent fluid velocity and the velocity of shock wave's movement, respectively. (a) A planar shock wave propagates at the speed of U_s in x direction through a fluid with x-directional velocity, with u varying in the shock-tangential direction. (b) Non-uniform shock-wave motion velocity distribution, sum of the fluid velocity and the velocity of the shock-wave propagation. (c) The shock-wave propagation's direction $\mathbf{n}$ is tilted by the shock-wave deformation, which results in positive and negative fluctuations of the pressure jumps for concave and convex regions, respectively.

wave position. Therefore, the propagation velocity becomes non-uniform due to the profile of the fluid velocity in front of the shock wave, causing shock wave to deform. When the shock wave is observed from the front, concave and convex shapes appear for the regions with negative and positive u, respectively, as shown in Figure 2.11. The shock wave's local propagation direction is normal to the local element of the shock wave. Thus, as the shock wave with the concave shape propagates, the concave region ($u < 0$), represented by a circle in Figure 2.11(c), becomes narrower, reducing the concave area projected on a plane perpendicular to the x direction. This decrease in area causes an increase in the local shock Mach number, along with an increase in the local pressure jump across the shock wave ($\Delta p' > 0$) [52]. Conversely, the convex region ($u > 0$) widens as the shock wave propagates, reducing the local pressure jump across the shock wave ($\Delta p' < 0$). These findings demonstrate that the local shock-wave motion induces pressure jump fluctuations across the shock wave, and the relation between u and the pressure jumps through the local shock-wave motion create the negative correlation shown in Figure 2.10. It should be noted that the initial values of the pressure jumps across the shock wave change as the shock wave deforms. Even if the velocity of the shock-wave movement is non-uniform, the pressure jump fluctuations shown in Figure 2.11(b) are not induced if the shock-wave surface is flat. The shock-wave deformation may advance depending on the turbulence's shearing motion, expressed by the velocity gradient ($\partial u/\partial y$ in Figure 2.11). Therefore, the shock-wave deformation becomes non-negligible for the direction of the local shock-wave propagation $\mathbf{n}$ after the shock wave undergoes the turbulent shear for a certain time period, causing the pressure jump fluctuations across the shock wave. This explains why the peak negative correlation is located behind the shock wave in Figure 2.10 rather than at the shock-wave position. Although this model explains some of the experimental results reported by Inokuma *et al.* [30], the correlation between local shock-wave deformation and local turbulence shear have not been confirmed.

In the present DNSs, the direction of a local shock-wave propagation is defined using the pressure gradient ∇p in the shock wave. The angle between ∇p and the y direction,

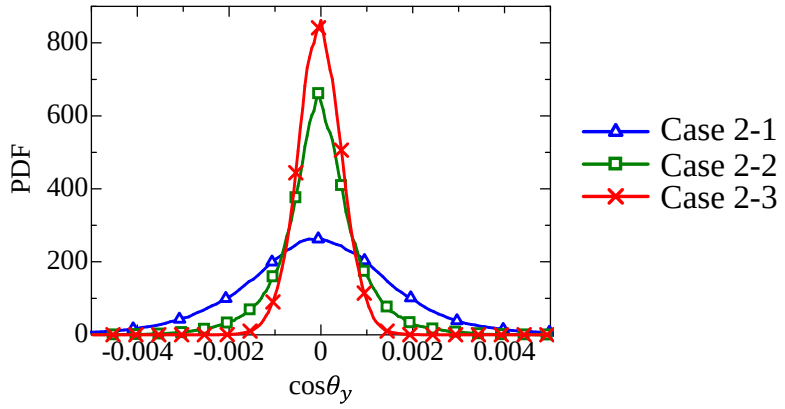

Figure 2.12. PDFs of $\cos\theta_y$.

θ_y, is evaluated via

$$\cos\theta_y = \frac{\partial p/\partial y}{|\nabla p|}, \tag{2.8}$$

at the shock-wave position x_s. Although the angle between ∇p and y is used in the present analysis, the same analysis can be applied to arbitrary directions perpendicular to x. The choice of the direction does not affect the statistical results because the problem considered here is statistically inhomogeneous only in the x direction. The y- and z-directional components of ∇p have non-zero values in case the shock wave deforms. Here, the pressure gradients in the initial HIT are neglected because the HIT pressure fluctuations are much weaker than the pressure jumps across the shock wave. Figure 2.12 shows the PDF of $\cos\theta_y$. Its profile of $\cos\theta_y \neq 0$ indicates that the interaction slightly deforms the shock wave. The probability with a large $|\cos\theta_y|$ increases as the shock wave weakens, suggesting that weaker shock waves undergo more deformation. This result supports those of the previous DNSs, where shock waves interact most with turbulence with a higher turbulent Mach number [27].

The local shear that deforms the shock wave in the model is represented by the gradient of u in y and z directions. In the present DNSs, the local shear concerning $\cos\theta_y$ is calculated using $\partial u/\partial y$ because the shock wave is normal to the x direction. Figure 2.13 shows the joint PDF of $\cos\theta_y(y,z;t)$ and $\partial u/\partial y(x_s,y,z;t=0)$, where $\cos\theta_y(y,z;t)$ is calculated in the shock wave at $x = x_s(t)$, and $\partial u/\partial y$ is taken from the

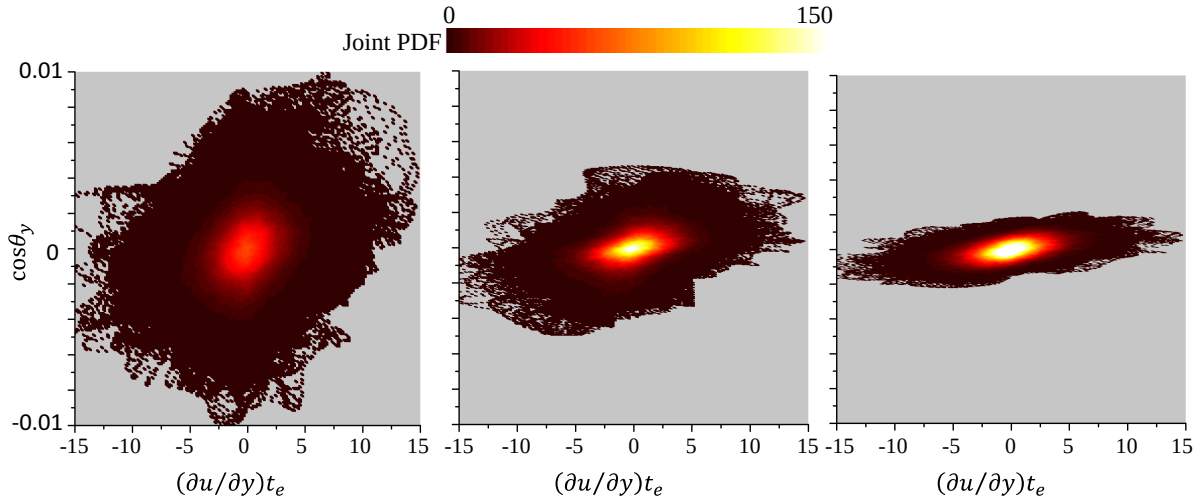

Figure 2.13. Joint PDFs between $\cos\theta_y$ and $\partial u/\partial y$ for (a) Case 2-1, (b) Case 2-2, and (c) Case 2-3 with 384^3 grid points. $\partial u/\partial y$ is normalized by the eddy turnover time $t_e = L/u'_{rms}$ of HIT.

HIT ($t = 0$). In all cases, $|\cos\theta_y|$ tends to increase with $|\partial u/\partial y|$, indicating that the degree of shock-wave deformation is related to the magnitude of $\partial u/\partial y$. This positive correlation between $\cos\theta_y$ and $\partial u/\partial y$ is consistent with the physical model presented in Figure 2.11.

The present model relates $\Delta p'$ to the spatial distribution of velocity with a large amplitude, where a large part of turbulent kinetic energy occurs. This explains why the pressure jump fluctuations are concentrated in large scales, as shown in Figure 2.8(b). Therefore, $\Delta p'$ is expected to be characterized by large scales. Scale dependence of the correlation between fluid velocity was investigated in an experimental study that used $Re_\lambda = 100 - 300$. The results showed that turbulent motions in the order of the integral length scale are important for the pressure jump fluctuations [30].

2.4 Conclusions

The fluctuations of local pressure jumps, $\Delta p'$, across the normal shock wave propagating through the HIT at a low turbulent Mach number are investigated via DNSs. Because of the low turbulent Mach number, the turbulence evolves much more slowly than the time scale of the shock-wave propagation. Here, the turbulent Mach number

$M_t = 2.96 \times 10^{-4}$ is fixed, while the shock Mach number M_s ranges between 1.1 and 1.5. The turbulent Reynolds number is 18 in all simulations.

Important characteristics of the pressure jumps across the shock wave are as follows:

- The PDF of $\Delta p'$ is well approximated by the Gaussian distribution.
- $\Delta p'$'s dependence on M_s is clearly observed at a M_s: $\Delta p'$ has a smaller rms value at lower M_s.
- Larger characteristic length scale is observed in the profile of $\Delta p'$ on the shock wave at lower M_s.

The correlations between pressure jump fluctuations across the shock wave and turbulence velocity fluctuations are as follows:

- $\Delta p'$ on a given shock ray is strongly affected by the turbulent velocity fluctuations near the same shock ray, but a weaker shock wave tends to be more influenced by turbulence far from the shock ray.
- The effects of velocity fluctuations at a given position become most significant in $\Delta p'$ after the shock wave propagates for a distance equal to the integral length scale.

These results resemble those of a previous experiment that studied the interaction between a spherical shock wave and grid turbulence [30].

Turbulence-induced shock-wave deformation is used to examine the effects of turbulence on $\Delta p'$, in which $\Delta p'$ relates to the curvature of the shock wave and the curvature locally alters the shock-wave propagation's direction. The model explains the relation between shock wave amplification or attenuation and the direction of fluid velocity in front of the shock wave. The joint PDF between the pressure gradient on the shock wave and the velocity gradient during turbulence indicates that turbulent shearing motions can tilt the shock wave's propagation direction. These results support the recent experimental findings concerning the finite response time within a turbulence-induced shock-wave modulation, confirmed for a weak spherical shock wave interacting with

grid turbulence at $Re_\lambda \approx$ 100-300 [30]. Although the present DNS is limited to the low turbulent Reynolds number $Re_\lambda = 18$, it demonstrates that the turbulence-induced shock-wave modulation's response time is finite (non-zero) even with higher shock Mach numbers.

Chapter 3

Statisitical characteristics of deformation of a normal shock wave propagating in a local turbulent region

3.1 Introduction

The DNSs of a normal shock wave propagating through a local turbulent region are used in this chapter to investigate shock-wave deformation and the effects of propagation distance. In the present DNSs, the turbulent region is localized in a quiescent fluid, and the interaction between the shock wave and turbulence occurs once the shock wave enters the turbulent region. This local turbulent region is generated by inserting HIT in the middle of the quiescent fluid. An initial transient process of the shock-wave modulation can be investigated by this setup. This is one of the unique points of the present DNSs because previous studies focused on the statistically stationary state of the interaction. In the present DNSs, both the initial transient process and the statistically stationary state of the shock-wave deformation induced by turbulence are investigated. The shock-wave deformation is defined as fluctuations of local shock-wave positions, which can provide quantitative properties. It should be noted that there is no mean

velocity in the turbulent region as there was for the DNSs in Chapter 2. Therefore, the effects of a mean velocity gradient on the mean shock Mach number, as reported in previous studies [33], [53], need not be considered. The analyses in this chapter rely on statistics concerning turbulence and the shock wave. Although the statistical approach is useful in understanding phenomena related to turbulence, turbulence statistics sometimes veil important characteristics of the instantaneous flow field. The present DNSs are used to investigate the statistical properties of the shock–turbulence interaction in a systematic manner by presenting the results as functions of important parameters; i.e., the turbulent Mach number and the shock Mach number.

3.2 Direct numerical simulations

3.2.1 Flow field and parameters of the shock wave and turbulence

Figure 3.1 shows a schematic view of the DNS of a normal shock wave propagating from a quiescent fluid to the turbulent region. The computational domain is a rectangular shape. Its size is $(L_x, L_y, L_z) = (32L_0, 4L_0, 4L_0)$, where the reference length

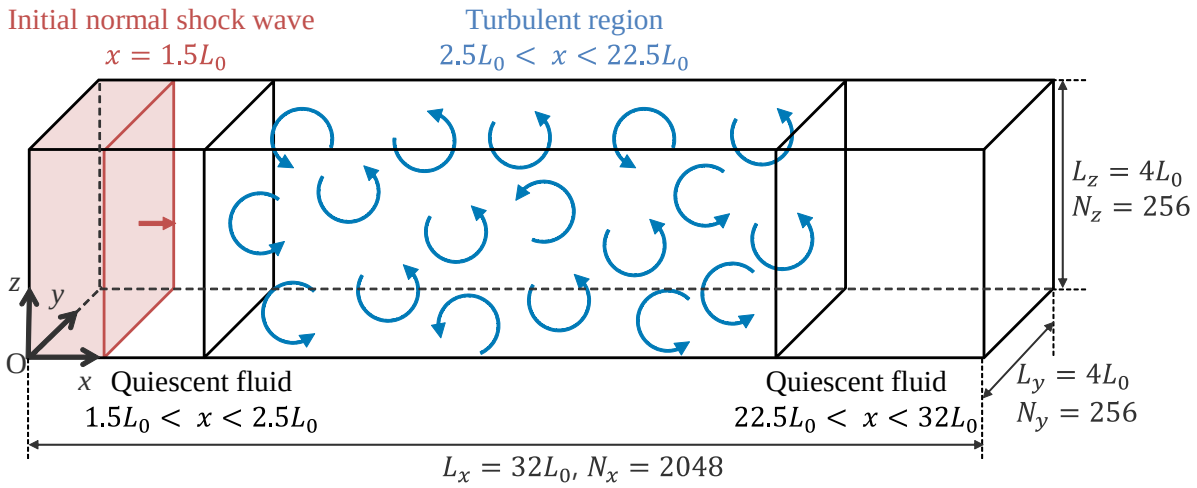

Figure 3.1. Schematic view of DNSs of a shock wave propagating from a quiescent fluid into a turbulent region.

scale L_0, defined later in Equation (3.1), is related to the integral length scale of turbulence, and the number of computational grid points is $(N_x, N_y, N_z) = (2048, 256, 256)$ in all simulations of the shock–turbulence interaction in this chapter. The values of the reference length scale L_0 are shown in Table 3.1. The definition of the coordinate is similar to the DNSs in Chapter 2. In the initial condition, the shock wave is located at $x = 1.5L_0$, while the turbulent region is between $2.5L_0 \leq x \leq 22.5L_0$. Therefore, there are interfaces between the turbulent region and the quiescent fluids on both sides of the turbulent region. This setup of the local turbulent region is the same as that considered in previous studies for a turbulent/non-turbulent interface [54]–[56]. After the start of the DNSs, the shock wave propagates in the quiescent fluid with time advancement. Then, the shock wave enters the turbulent region, and shock–turbulence interaction occurs. In the DNSs, time is advanced until the shock wave reaches the far side of the local turbulent region. The DNS methodology and subsequent analyses are summarized below.

1. Run a DNS of HIT with linear forcing and store the instantaneous flow field at various time steps.
2. Run a DNS of the shock wave propagating in a quiescent fluid and store the flow variables around the shock wave.
3. Generate the initial condition for the DNS of the shock–turbulence interaction from the simulations in steps 1 and 2.
4. Run the DNS of the shock–turbulence interaction. Repeat this DNS for different realizations of HIT using the instantaneous flow field at different time steps as shown in step 3.
5. Perform statistical analysis on the instantaneous flow fields saved in the DNS of the shock–turbulence interaction.

Details of steps 1 and 2 are explained in Sections 3.2.3 and 3.2.4, respectively. The flow considered in step 4 is described below, and the detailed numerical method is presented in Section 3.2.2. The method to calculate the statistics of the shock–turbulence

Table 3.1. Parameters of the simulations of the shock–turbulence interaction.

Case	M_s	M_t	$M_t/(M_s-1)$	$M_t^2/(M_s^2-1)$	Re_λ	L/L_0	λ/L_0	η/L_0	L_0[m]
3-1	1.3	0.13	4.2×10^{-1}	2.3×10^{-2}	64	0.56	0.18	0.011	2.4×10^{-4}
3-2	1.3	0.063	2.1×10^{-1}	5.7×10^{-3}	71	0.70	0.19	0.012	4.8×10^{-4}
3-3	1.3	0.011	3.7×10^{-2}	1.8×10^{-4}	59	0.74	0.17	0.012	2.4×10^{-3}
3-4	1.1	0.011	1.1×10^{-1}	6.0×10^{-4}	59	0.74	0.17	0.012	2.4×10^{-3}
3-5	1.01	0.011	1.1×10^{0}	6.2×10^{-3}	60	0.74	0.17	0.012	2.4×10^{-3}

interaction is presented in Section 3.3.

Table 3.1 summarizes the parameters of the shock wave and turbulence. The turbulence characteristics are calculated from volume averages in the turbulent region. The DNSs are performed for five cases with different sets of a shock Mach number M_s and a turbulent Mach number M_t. Cases 3-1 to 3-3 are conducted for $M_t = 0.13, 0.063$ and 0.011 with a constant shock Mach number $M_s = 1.3$, which are used to investigate turbulent Mach number dependence. The effects of the shock Mach numbers are observed for Cases 3-3 to 3-5 at $M_s = 1.01$, 1.1, and 1.3, with a constant turbulent Mach number of $M_t = 0.011$. Previous DNS studies have shown that interaction with turbulence causes the shock wave to break [15], [26], [27]. However, with the setup shown in Table 3.1, it is expected that the shock wave will retain its surface without any breakage.

In Section 3.3, statistics of the shock wave are often presented against $M_t/(M_s-1)$ and $M_t^2/(M_s^2-1)$, the values of which are shown in Table 3.1. The table also presents the turbulent Reynolds number Re_λ, the integral length scale L, the Taylor microscale λ, and the Kolmogorov length scale η. These statistics are obtained in HIT before the interaction, and the quiescent fluid surrounding the turbulent region in Figure 3.1 is not used as a statistical sample. All simulations are conducted for the turbulent Reynolds number Re_λ of 60-70. The results indicate that dependence on Re_λ is weak compared the dependence on M_s and M_t. The computational grid size Δ is $0.016L_0$, which is equivalent to 1.4η. The grid spacing is uniform in the entire computational domain. Prior DNS studies on turbulence have used computational grids of similar sizes [57]–[60].

A widely used criterion for evaluating the spatial resolution of DNS with a spectral method is $\Delta/\eta \leq 2.1$ [37]. A resolution better than $\Delta/\eta = 2.1$ is used in the present DNSs because the DNS code is based on the high-order finite volume method, which does not have a spectral resolution. However, the spatial resolution is lower than the DNSs in Chapter 2. Therefore, it is necessary to verify this chapter's results concerning grid spacing dependence. The effects of grid spacing are discussed in the Appendix.

The local turbulent region is generated using HIT obtained via additional DNSs, as explained in Section 3.2.3. For each condition, the simulations of the shock–turbulence interaction are repeated five times using instantaneous HIT flow data at different time steps. An additional five simulations are performed only for Case 3-1 to check statistical convergence. The statistics in Case 3-1 are calculated using 10 simulations. For assessing statistical errors, results from two independent sets of five simulations are presented. The degree of statistical convergence is similar in all cases because the computational domain size is the same in all simulations. Therefore, the statistical errors in Cases 3-2 to 3-5 are estimated from Case 3-1 by assuming that the fractional error is the same in all cases. Here, the fractional error in Case 3-1 is defined as the difference in statistics between the five and ten simulations. The estimated errors are shown with error bars in figures in Section 3.3. As shown in Section 3.3, the error due to statistical convergence is minor and does not affect this chapter's results. Simulations with a lower turbulent Reynolds number using a single snapshot of turbulence are also conducted, wherein the effects of the spatial resolution are evaluated for the statistics of the shock-wave positions. Issuees of statistical convergence and spatial resolution are also discussed in the Appendix.

3.2.2 Governing equations and numerical schemes

The governing equations and numerical schemes observed here are similar to the DNSs in Chapter 2. The governing equations are three-dimensional, compressible Navier–Stokes equations represented by Equations (2.1) to (2.3), with the equation of state for a perfect gas Equation (2.4) and the Stokes hypothesis is Equation (2.5). The

DNS code is parallelized with the message passing interface (MPI). The computational domain is divided into y and z directions. The subdomains elongated in the x direction are treated in each MPI process. The validations of the DNS code are explained in Section 2.3.1. DNSs of the shock–turbulence interaction are performed using a high-performance computing system at Nagoya University. The code is based on the finite-volume method with a shock-capturing scheme. Spatial discretization of inviscid terms is based on the Roe flux difference splitting with a 5th-order WENO scheme [26]. The other terms are calculated using the 6th-order central difference scheme. Time advancement is based on the 4-stage, 4th-order Runge–Kutta method.

Numerical dissipation caused by the Roe flux splitting may dump small-scale fluctuations during turbulence. The statistics in front of the shock wave during the shock-wave propagation are monitored; the effects of numerical dissipation are negligible for the statistics of turbulence during shock-wave propagation. This is confirmed by the skewness of the velocity derivative, as described in Chapter 2. The skewness hardly changes with time, and the present numerical scheme does not cause artificial decay of turbulence during shock-wave propagation. Note that the propagation time is longer than those in Chapter 2. Artificial decay likely does not occur because the spatial resolution, $\Delta/\eta = 1.4$, is better than the widely used criterion of $\Delta/\eta = 2.1$ [37].

The Dirichlet boundary condition is applied to the physical variables behind the shock wave at $x = 0$, and the boundary at $x = 32L_0$ is treated with the zero-gradient condition. As mentioned in Chapter 2, once the shock Mach number is specified as a computational parameter, physical variables behind the shock wave can be calculated via Rankine-Hugoniot relations using the shock Mach number and corresponding variables in front of the shock wave. Here, the initial flow state in front of the shock wave is specified as an initial condition explained in Section 3.2.3. It is also mentioned in Chapter 2 that these conditions are not non-reflecting boundary conditions. Therefore, sponge zones with a 2nd-order low-pass filter are employed near the boundaries in the x direction. The filter dumps the pressure waves toward the boundaries, thereby preventing the reflected waves from affecting the shock–turbulence interaction. Periodic boundary conditions

are used for y and z directions.

3.2.3 Initial conditions of turbulence

The local turbulent region is generated by performing additional DNSs of compressible HIT with linear forcing [61], which only forces solenoidal components of the velocity vector. The initial conditions are divergence-free, random velocity fields. The density field is uniform with a value of $\rho = \rho_0 = 1.17$ [kg/m^3]. Volume-averaged pressure and temperature taken in the whole HIT are $\langle p \rangle = 1.013 \times 10^5$ [Pa] and $\langle T \rangle = 300$ [K], respectively. The random velocity field in the physical space can be obtained by applying inverse Fourier transform to velocity vectors in the wavenumber space with a random phase. Here, the divergence-free condition is enforced in the phase space. Pressure fluctuations are calculated from the velocity fluctuations by solving the Poisson equation for pressure under the divergence-free condition in the velocity field [61], and then temperature fluctuations are calculated using the equation of state. The velocity in the wavenumber space is assumed to have a turbulent kinetic energy spectrum of $E(k)$, given in Ref. [37] :

$$E(k) = C\varepsilon_0^{2/3} k^{-2/3} f_L(kL_0) f_\eta(k\eta_0), \tag{3.1}$$

$$f_L(kL_0) = \left(\frac{kL_0}{[(kL_0)^2 + c_L]^{1/2}} \right)^{\frac{5}{3}+A}, \tag{3.2}$$

$$f_\eta(k\eta_0) = \exp\{-\beta([(k\eta_0)^4 + c_\eta^4]^{\frac{1}{4}} - c_\eta)\}, \tag{3.3}$$

where $C = 1.5$, $\beta = 5.2$, $A = 2$, $c_L = 6.78$, and $c_\eta = 0.4$. Here, k is the wavenumber, ε_0 is the turbulent kinetic energy dissipation rate used as a parameter in the model spectrum, $L_0 = (\sqrt{3/2}u_0)^3/\varepsilon_0$ is related to the integral length scale, u_0 is the initial rms value of velocity fluctuations, and $\eta_0 = (\langle \nu \rangle^3 \langle \rho \rangle / \varepsilon_0)^{1/4}$ is the initial Kolmogorov length scale ($\langle \nu \rangle$ in which kinematic viscosity is determined by $\langle T \rangle$ and $\langle \rho \rangle (= \rho_0)$). The parameters are calculated from the given turbulent Mach number and turbulent Reynolds number, which can be written as $M_t = \sqrt{3}u_0/\sqrt{\gamma R \langle T \rangle}$ and $Re_\lambda = \sqrt{15}u_0^2(\langle \nu \rangle \varepsilon_0)^{-1/2}$ in HIT, respectively. L_0 and u_0 are used as reference length and velocity scales, respectively, in the simulations of the shock–turbulence interaction.

DNSs of HIT are performed using a modified version of the DNS code that was previously used for supersonic turbulent boundary layers and planar jets [62]–[64]. Here, the 8th-order central difference scheme and the 5-stage, 4th-order Runge–Kutta scheme are adapted for spatial and temporal discretization. Following Wang *et al.* [65], the 10th-order low-pass filter [66] is applied to simulated variables at the end of each time step to prevent the growth of unphysical fluctuations inherently arising from the central difference scheme. The computational domain size is $(4L_0)^3$, and the number of grid points is 256^3, where the grid spacing is uniform. From the initial condition, time is advanced until the turbulence reaches a statistically stationary state. The turbulent Mach number, turbulent Reynolds number, mean temperature, and mean pressure hardly change from the initial condition, whereas compressibility effects, such as density fluctuations and dilatation, emerge with time and the initial velocity field is purely solenoidal.

The local turbulent region in Figure 3.1 is generated by the method proposed by Teixeira *et al.* [54], which inserts HIT in the middle of a quiescent fluid whose pressure and temperature are 1.013×10^5 Pa and 300 K, respectively. The length of the local turbulent region is $20L_0$. DNSs of HIT are conducted using a periodic box. Therefore, the turbulent region with a length of $20L_0$ is generated from a single snapshot of the HIT using the periodicity. Periodic effects on the statistics related to the shock–turbulence interaction do not appear because ensemble averages are taken for the simulations with different turbulence snapshots. The boundaries between the turbulent region and the quiescent fluids appear at $x = 2.5L_0$ and $22.5L_0$, as shown in Figure 3.1. Variables $Q = \rho, \rho u_i$, and e are smoothly adjusted between the two regions by applying a smoothing function as follows:

$$F[Q(x,y,z)] = Q_L + [Q(x,y,z) - Q_L]g_1(x)g_2(x), \tag{3.4}$$

$$g_1(x) = \frac{1}{2} + \frac{1}{2}\tanh\left(\frac{x - x_{t1}}{\delta_t}\right), \tag{3.5}$$

$$g_2(x) = \frac{1}{2} - \frac{1}{2}\tanh\left(\frac{x - x_{t2}}{\delta_t}\right), \tag{3.6}$$

where Q_L is a constant value of the variable in the quiescent fluid, $x_{t1} = 2.5L_0 + \delta_t/2$ and $x_{t2} = 22.5L_0 - \delta_t/2$ define the regions where the smoothing function is applied, and

$\delta_t = 10\Delta$ is the thickness of the buffer regions. $g_1(x)g_2(x)$ is equal to 1 in most parts of the turbulent region and decreases to 0 at the edges of the turbulent region. Therefore, the smoothing function ensures that the variables smoothly vary between the turbulence and the quiescent fluid, while the turbulent region retains the original flow field obtained in the DNSs of HIT. Once the DNSs of the shock–turbulence interaction begin, the buffer regions also evolve with time. As temporal evolution obeys the compressible Navier–Stokes equations, the mass, momentum, and energy conservations are still held in the buffer regions.

3.2.4 Initial conditions of shock waves

In numerical simulations of the shock–turbulence interaction, profiles of conservative variables of the shock wave are inserted at around $x = 1.5L_0$, and the numerical solution for the shock wave is obtained by simulating the normal shock wave propagating in the quiescent fluid. Here, the computational domain size is $(L_x, L_y, L_z) = (16L_0, 4L_0, 4L_0)$, and the number of grid points is $(N_x, N_y, N_z) = (1024, 256, 256)$. Grid spacing is uniform. Spatial resolution, numerical schemes, and boundary conditions are the same as those used in the DNSs of the shock–turbulence interaction. The simulations of the shock wave are initialized with the profiles of variables $Q = \rho$, ρu_i, and e, as shown

$$Q(x, y, z) = Q_F + (Q_B - Q_F)\left[\frac{1}{2} - \frac{1}{2}\tanh\left(\frac{x - x_{s0}}{\delta_s}\right)\right], \tag{3.7}$$

where the subscripts F and B represent values in front of and behind the shock wave, respectively. The flow state in front of the shock wave, Q_F, is the same as that in the quiescent fluid in the simulations of the shock–turbulence interaction. Then, Q_B is calculated from Q_F and M_s using Rankine-Hugoniot relations. The position of the shock wave is $x_{s0} = 1.5L_0$, and the initial thickness of the shock wave is $\delta_s = 10\Delta$.

Equation (3.7) represents a compression wave without discontinuity. The smoothed profile given by Equation (3.7) is used as the initial condition because numerical oscillations can occur behind the shock wave if variables discontinuously change over one computational grid point. The density profiles on the centerline of the computational

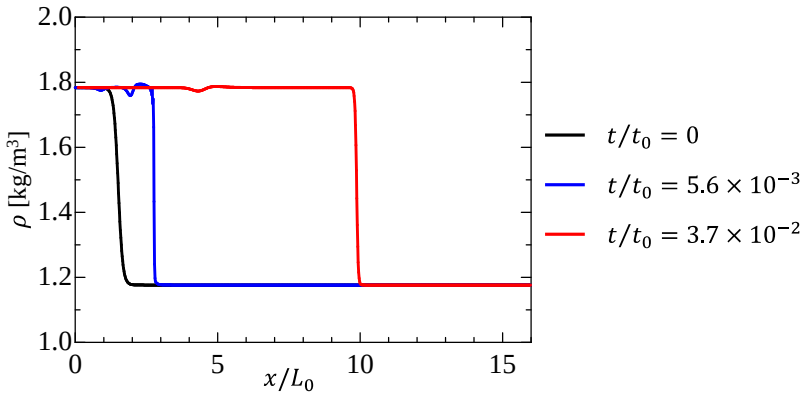

Figure 3.2. Density profiles on the center line of the computational domain at three different time steps in the propagation process.

domain in the case of $M_s = 1.3$ at the three different time steps are shown in Figure 3.2. The initial density profile is represented by a black line in Figure 3.2. As time advances in the simulation, the compression wave propagates in the x direction. The numerical oscillations are caused by the initial condition in the early propagation process, as represented by a blue line in Figure 3.2. Conversely, the gradient of the variables across the wave becomes steeper during the propagation process. Then, the compression wave converges to a normal shock wave that can be treated using numerical schemes. Time advances until the jumps of physical variables across the shock wave become independent of time. The red line in Figure 3.2 represents the density profile after time advancement. Profiles of the variables around the shock wave are taken from the simulation and inserted at around $x = 1.5L_0$ as the initial DNS condition for the shock–turbulence interaction.

3.3 Results and discussion

3.3.1 Shock wave propagation from quiescent fluid to local turbulent region

Figure 3.3 visualizes of velocity in the x direction on the x-y plane at five different

time steps in Case 3-1. Here, time is normalized by the reference time scale of the simulations $t_0(= L_0/u_0)$. The shock wave is represented by the velocity discontinuity. The shock-wave deformation occurs after the shock wave enters the local turbulent region. The small deformation is observed at the beginning of the interaction, as shown in Figure 3.3(b). The deformation grows in Figures. 3.3(c-e) after the shock wave propagates during turbulence. This tendency has been reported in previous experimental studies on a normal shock wave interacting with grid turbulence, wherein shock-surface deformation increases with interaction length [34]. Figure 3.4 shows the density (ρ) profile on the same x-y plane as in Figure 3.3. The shock wave is observed as a density-discontinuous

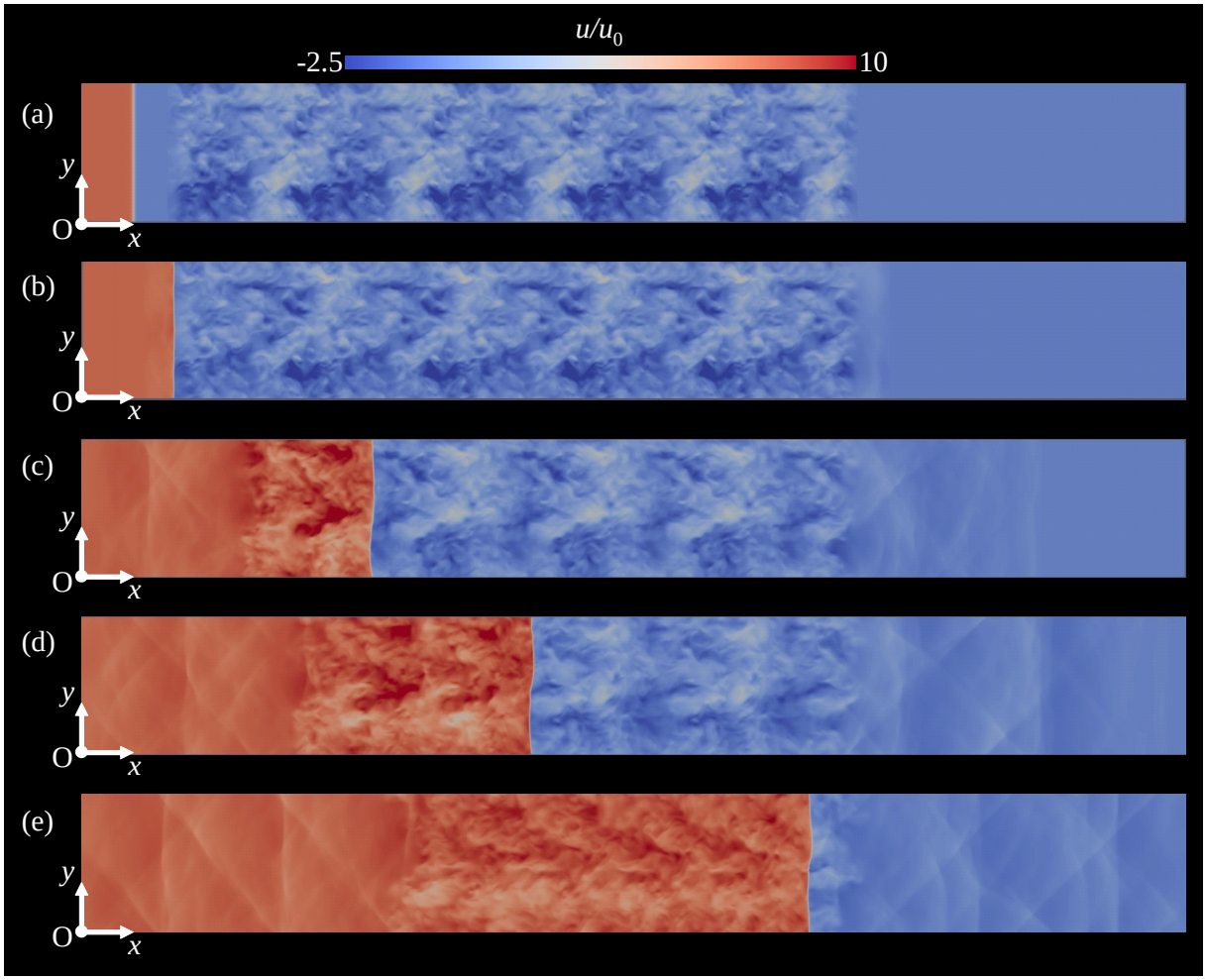

Figure 3.3. Two-dimensional profiles of velocity in x direction, u/u_0, on an x-y plane of $z = 2L_0$ in Case 3-1 at (a) $t/t_0 = 0$, (b) $t/t_0 = 0.05$, (c) $t/t_0 = 0.31$, (d) $t/t_0 = 0.52$, and (e) $t/t_0 = 0.78$.

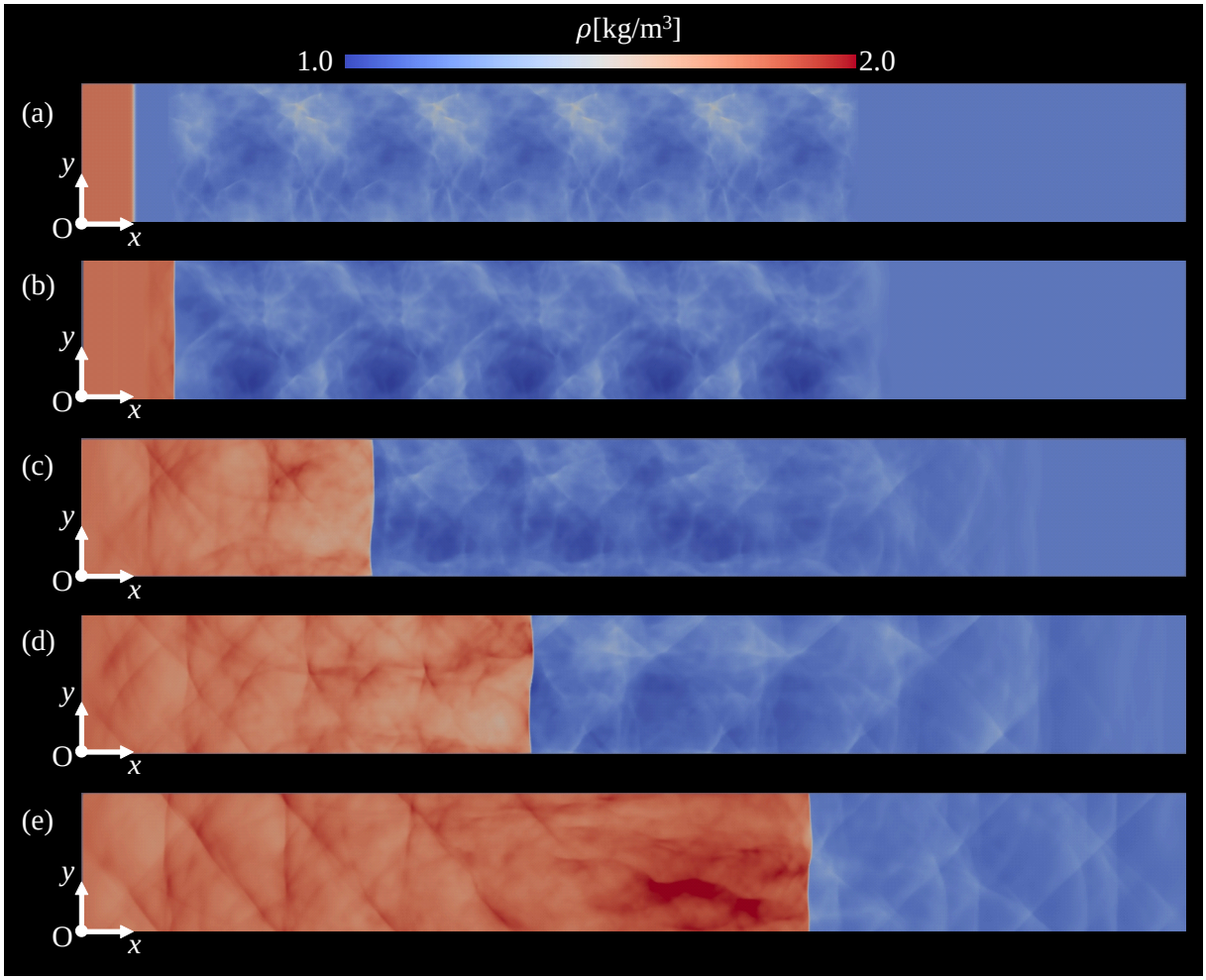

Figure 3.4. Two-dimensional profiles of density, ρ [kg/m^3], on the same x-y plane as in Figure 3.3 at (a) $t/t_0 = 0$, (b) $t/t_0 = 0.05$, (c) $t/t_0 = 0.31$, (d) $t/t_0 = 0.52$, and (e) $t/t_0 = 0.78$.

jump. There are density fluctuations during turbulence in Case 3-1 because of the relatively high turbulent Mach number. These density fluctuations are still weak compared with the density jump of the shock wave, and the broken part of the shock wave cannot be seen in the visualizations as expected.

Figure 3.5 shows 3D visualization of the deformed shock wave surface located at $x \approx 19L_0$ in Case 3-1. The shock wave is visualized with large negative pressure gradient of $\partial p/\partial x$. 3D visualization is widely used in previous numeircal studies. Conversely, most experimental studies observe shock-wave deformation via shadowgraph or schlieren visualizations [28], [34], [67]. Information acquired this way is integrated along a light path,

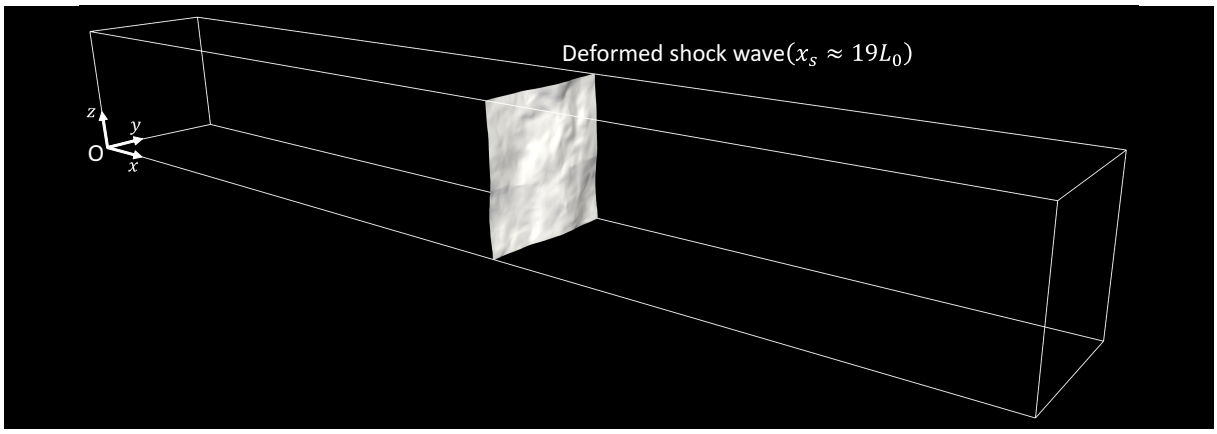

Figure 3.5. 3D visualization of the deformed shock wave located at $x \approx 19L_0$ in Case 3-1.

and it is difficult to relate the visualizations to the local geometry of the shock surface. Reproducing the shadowgraph visualizations using numerical spatial data can aid future experimental studies of the shock-turbulence interaction. Shadowgraph visualizations can be constructed from the three-dimensional instantaneous flow fields in DNSs. The numerical shadowgraph visualizations assume a paraxial hypothesis and a perfectly parallel incident light ray, whose intensity is denoted by I_0 [68]. The incident light ray is parallel to the z direction and passes through the computational domain from $z = 0$ to L_z. Diffraction of the light ray induced by density fluctuations results in light intensity fluctuations, $\Delta I(x, y) = I(x, y) - I_0$. Numerical shadowgraph visualizations can be obtained by visualizing $\Delta I(x, y)/I_0$, calculated as

$$\frac{\Delta I}{I_0} = -l\left(\frac{\partial \varepsilon_x}{\partial x} + \frac{\partial \varepsilon_y}{\partial y}\right), \tag{3.8}$$

$$\varepsilon_i(x, y) = \frac{G}{n_0}\int_0^{L_z} \frac{\partial \rho}{\partial x_i} dz, \tag{3.9}$$

where ε_i is the deviation of the light ray in the i-direction ($i = x, y$), $G = 2.3 \times 10^{-4}[\mathrm{m}^3/\mathrm{kg}]$ is the Gladstone–Dale constant, $n_0 = 1 + \rho_0 G$ is the refraction index for air with $\rho_0 = 1.17$ [kg/m^3], and l is the distance between the end of the computational domain and a virtual screen on which the shadowgraph visualization is projected. Figure 3.6 shows the results of numerical shadowgraph reproductions, in which shock waves are located at $x \approx 3.3L_0$, $9.0L_0$, or $19.0L_0$. The shock waves are observed as a pair

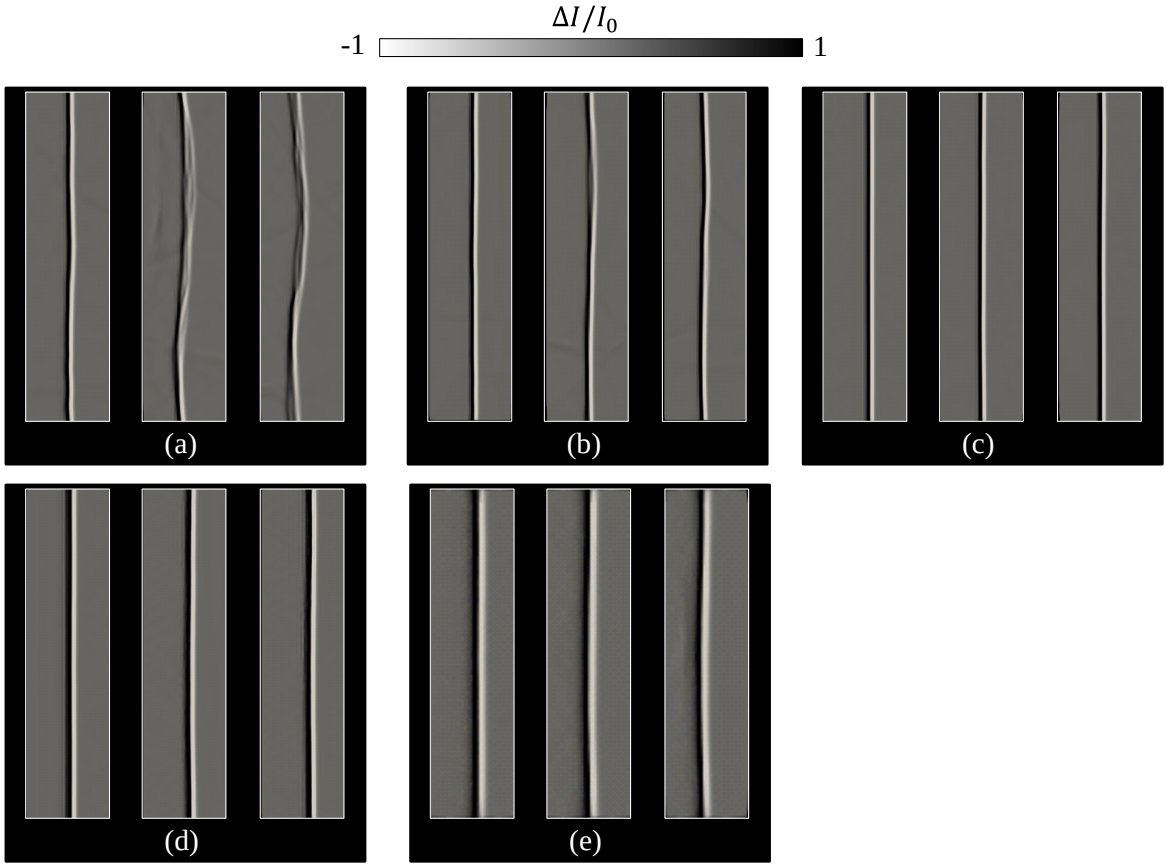

Figure 3.6. Numerical shadowgraph visualizations for the shock wave located at $x \approx 3.3L_0$, $x \approx 9.0L_0$, and $x \approx 19L_0$ from left to right in each figure (a) Case 3-1 ($l/L_0 = 1$), (b) Case 3-2 ($l/L_0 = 1$), (c) Case 3-3 ($l/L_0 = 1$), (d) Case 3-4 ($l/L_0 = 5$), and (e) Case 3-5 ($l/L_0 = 100$).

of black and white vertical lines. Comparing Figures 3.6(a-c), it is evident that the shock-wave deformation grows as M_t increases from (c) to (a). This M_t dependence is consistent with previous DNS studies on the shock–turbulence interaction [26], [27]. The largest deformation appears at $x \approx 19L_0$ in Figure 3.6(a), where the deformed shock wave appears as multiple dark and white lines. Similar observations are reported in experimental shadowgraph visualizations taken for a normal shock wave interacting with grid turbulence [34]. Turbulence in Figures 3.6(c-e) has $M_t = 0.011$ with different values of M_s. Shock-wave deformation increases with lower shock Mach numbers. Although the shock wave is largely deformed by the interaction, the broken part of the shock wave does not appear in the shadowgraph visualizations.

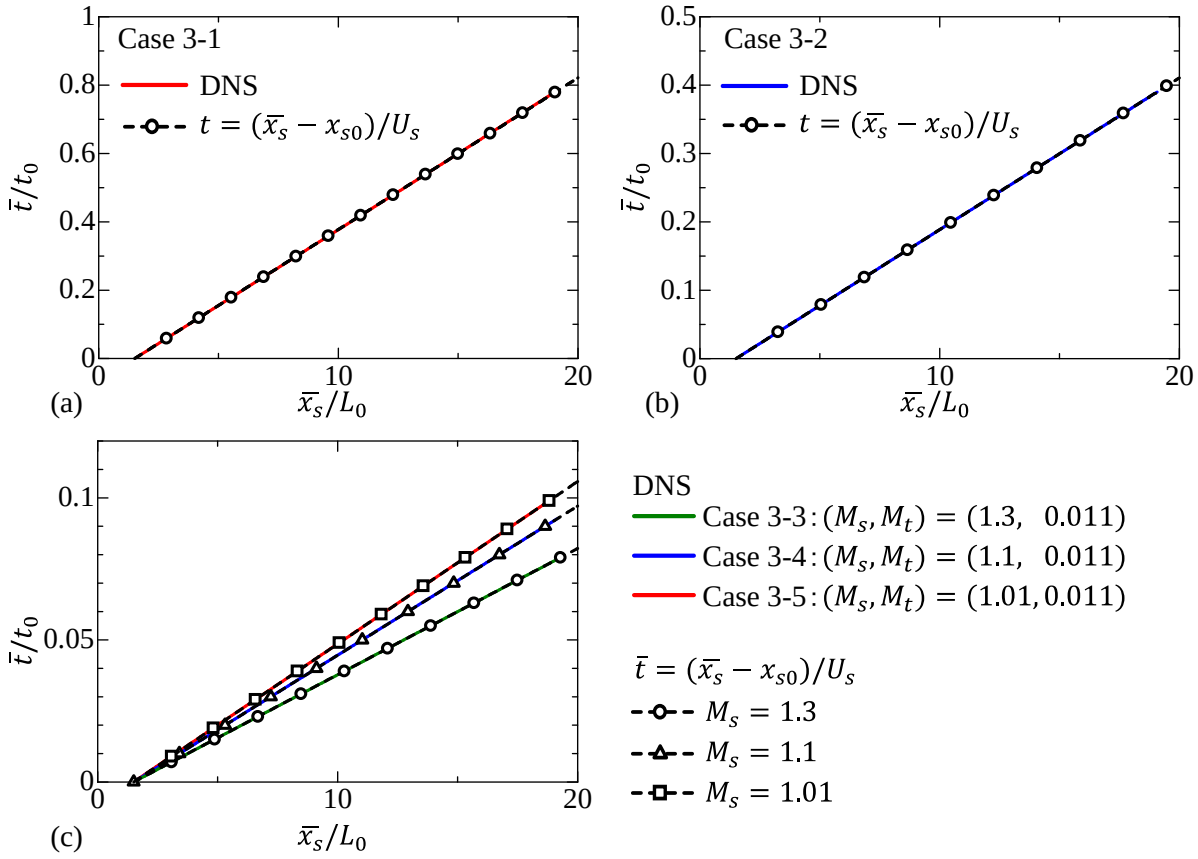

Figure 3.7. Relation between mean shock-wave positions $\overline{x_s}$ and time t: (a) Case 3-1 ($M_t = 0.13$); (b) Case 3-2 ($M_t = 0.063$); (c) Cases 3-3, 3-4, and 3-5 ($M_t = 0.011$).

3.3.2 Statistics of the local shock-wave position

In this chapter, the local shock-wave position x_s is detected using a local pressure gradient in x direction as per $\partial p/\partial x$, which is largely negative. Hereafter, $p_x(x)$ is the profile of $p_x \equiv \partial p/\partial x$ along the x direction for each (y, z) position. The x_s is defined as the position where $p_x(x)$ attains its largest negative value. Practically, the 2nd-order Lagrange interpolation is applied to $\partial p/\partial x$ around the computational grid points, where $\partial p/\partial x$ takes the largest negative value to obtain the minimum value of $p_x(x)$ in its continuous profile. The minimum value in the continuous profile is used to identify x_s, which is obtained as a function of y, z, and t by repeatedly applying this procedure for all (y, z) positions in each snapshot with different time steps. The present definition

of the local shock-wave position is related to that with a local dilatation of θ used in previous studies [26], [27]. It is expected that either quantity will be able to detect the shock wave because both have a large negative shock wave peak. Statistics of $x_s(y,z;t)$ are calculated as functions of t by taking averages in the y and z directions as well as ensemble averages of the simulations.

Figure 3.7 shows the relation between the mean shock-wave position $\overline{x_s}(t)$ and time t, whose reference values are L_0 and $t_0(=L_0/u_0)$. Here, t_0 is the time scale of turbulence, which depends on M_t. The plots of $\overline{x_s}/L_0$ against t/t_0 are different even for the same shock Mach number in Cases 3-1 and 3-2 because the reference time scale t_0 differs depending on M_t. The figure also shows a linear relation, $\overline{x_s} = U_s t + x_{s0}$, considering a constant propagation velocity of the shock wave, U_s. The difference between the results of the DNSs and the linear relation is smaller than 0.5 % in all cases. Therefore, U_s is hardly changed with time from the initial propagation velocity, and the mean position of the shock wave is well-predicted by the linear relation $\overline{x_s} = U_s t + x_{s0}$ for all cases. The mean propagation velocity is hardly affected by the interaction.

The shock-surface deformation is defined as the fluctuations of the local shock-wave positions $x'_s(y,z;t) = x_s(y,z;t) - \overline{x_s}(t)$ in this chapter. Figures 3.8(a) and (b) show the rms values of x'_s, $x'_{s,rms}$, normalized by η, plotted against the mean shock-wave position $\overline{x_s}/L_0$. Here, η is the Kolmogorov length scale of intial turbulence. Cases 3-1 to 3-3 with $M_s = 1.3$ are compared in Figure 3.8(a), whereas Cases 3-3 to 3-5 with $M_t = 0.011$ are compared in Figure 3.8(b). The shock wave at $\overline{x_s}/L_0 \geq 2.5$ is located within the turbulent region. $x'_{s,rms}$ starts increasing once the shock wave enters the turbulent region at $\overline{x_s} \approx 2.5L_0$ in all cases. However, $x'_{s,rms}$ becomes almost independent from the propagation distance (time) for $\overline{x_s} \geq 12L_0$, with a peak value around $\overline{x_s} = 7.5L_0$, except in Case 3-5. For Case 3-5, whose shock Mach number is smallest, $x'_{s,rms}$ slowly increases with time until the end of the simulation; however, the increase rate for $\overline{x_s} \geq 15L_0$ is very small. Normalized values of $x'_{s,rms}/\eta$ in the stationary state depend on the shock and turbulent Mach numbers. The results for Cases 3-1 to 3-3 with $M_s = 1.3$ suggest that $x'_{s,rms}$ increases with the turbulent Mach

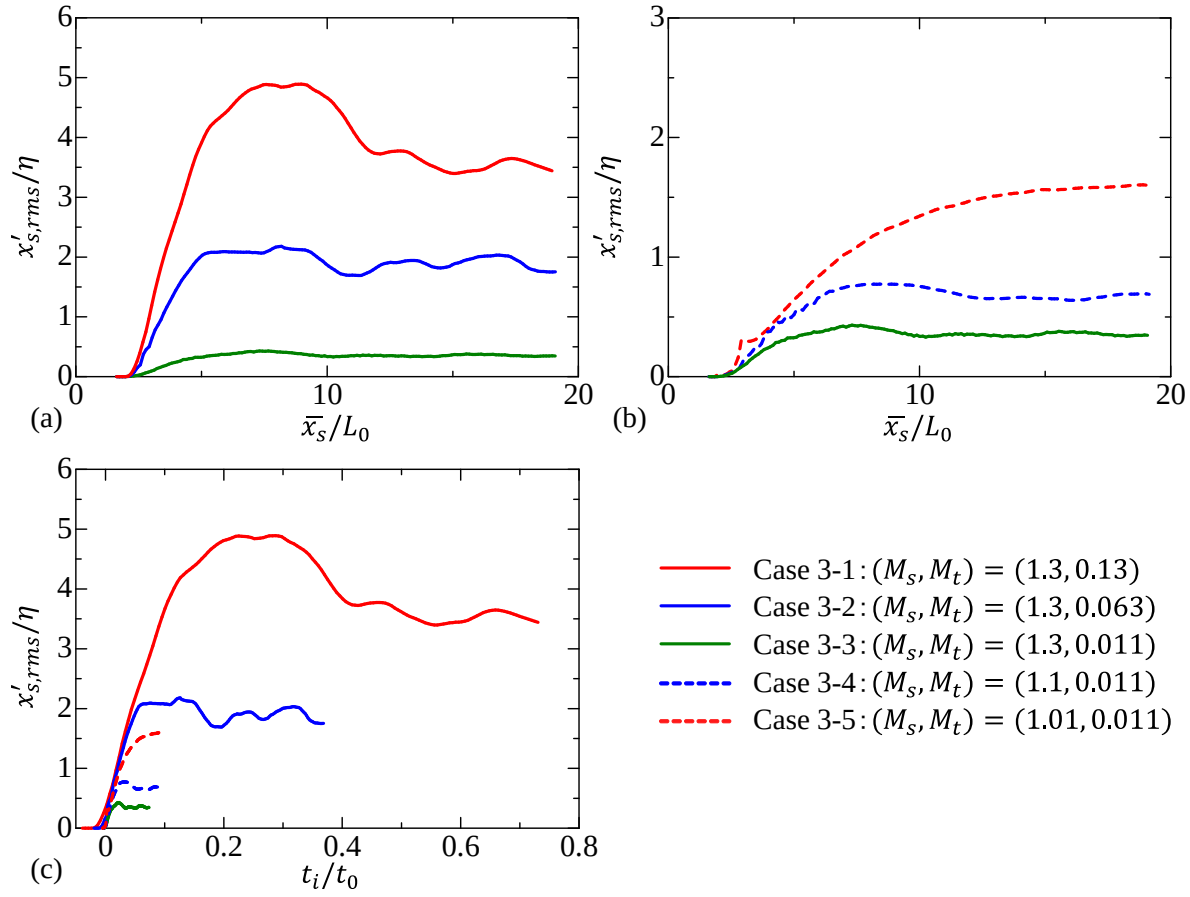

Figure 3.8. The rms values of the fluctuations of the shock-wave positions, $x'_{s,rms}$, plotted against (a,b) the mean position $\overline{x_s}/L_0$ and (c) the interaction time t_i/t_0. Here, $x'_{s,rms}$ is normalized by the Kolmogorov length scale η during turbulence under the initial condition: (a) Turbulent Mach number dependence for $M_s = 1.3$ (Cases 3-1 to 3-3); (b) Shock Mach number dependence for $M_t = 0.011$ (Cases 3-3 to 3-5).

number. For Cases 3-3 to 3-5 with $M_t = 0.011$, $x'_{s,rms}$ decreases with the shock Mach number. $x'_{s,rms}$ has a tendency to attain the stationary state late in the interaction in all cases, suggesting that the stationary state might be caused by the stability of the shock-wave surface against small deformation [69]. The statistical convergence and the effects of spatial resolution are mentioned in the Appendix. Figure 3.8(c) plots $x'_{s,rms}/\eta$ against normalized interaction time t_i/t_0, defined as the time over which the shock wave propagates in the turbulent region $t_i = (x_s - 2.5L_0)/U_s$. The relation between $x'_{s,rms}/\eta$ and t_i/t_0 confirms that the time it takes for the shock wave to reach the stationary

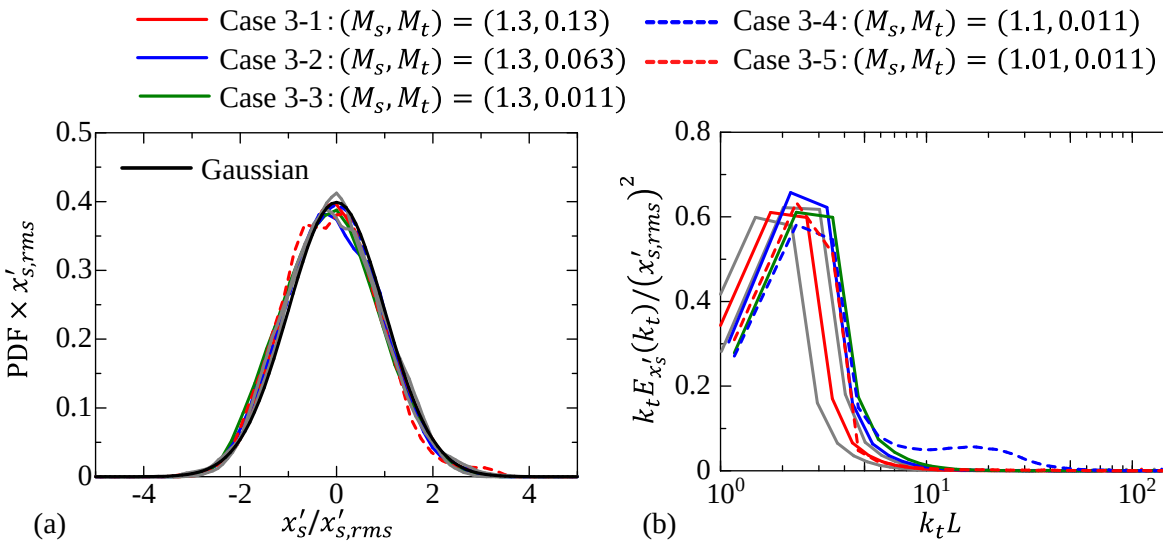

Figure 3.9. (a) Probability density functions (PDFs) of x'_s normalized by $x'_{s,rms}$. (b) Energy spectra of x'_s, $E_{x'_s}(k_t)$, in an area-preserving form, where k_t is a wavenumber in the transverse direction of the shock wave. Grey lines are obtained via two independent sets of five simulations in Case 3-1.

state differs in each case. However, the initial non-dimensional growth rate of $x'_{s,rms}/\eta$ is similar in all cases. These results imply the importance of the interaction length on shock-wave deformation similar to the experimental results reported by Tamba *et al.* [34]. However, these results cannot be quantitatively compared with experimental results because there are no quantitative data about the effects of interaction length on shock-wave deformation. Comparison between numerical simulations and experiments is one of the biggest problems of studies of shock–turbulence interaction.

Hereafter, the time average is applied to improve statistical convergence because $x'_{s,rms}$ becomes almost independent of time after the shock wave propagates for a long period. The average is taken over time periods for which the mean shock-wave position $\overline{x_s}$ is located between $13L_0$ and $19L_0$. Figure 3.9(a) shows PDFs of x'_s normalized by $x'_{s,rms}$, which agrees well with the Gaussian profile in all cases similar to the PDFs of $\Delta p'$ discussed in Section 2.3.2. Previous studies have reported that various quantities of PDFs concerning shock-wave characteristics, such as fluctuations in pressure and density jumps across the shock wave, exhibit good agreement with the Gaussian

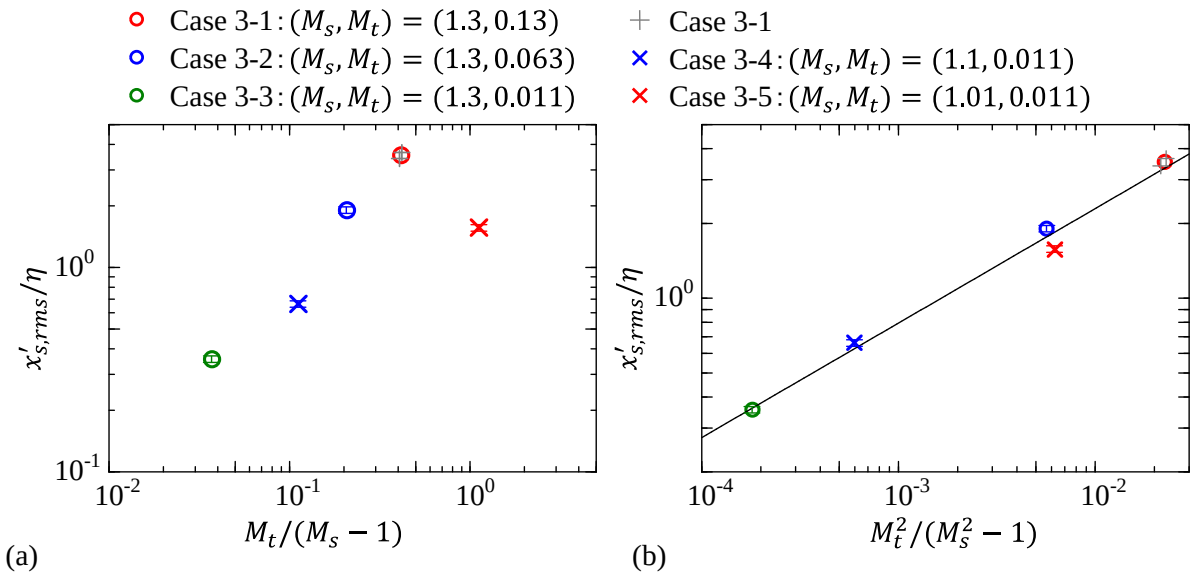

Figure 3.10. $x'_{s,rms}/\eta$ plotted against (a) $M_t/(M_s-1)$ and (b) $M_t^2/(M_s^2-1)$. A solid line in (b) represents a power law obtained using the least squares method. Gray "+" symbols are obtained by two independent sets of five simulations for Case 3-1. Error bars for Cases 3-2 to 3-5 represent 3.3% of the fractional error in $x'_{s,rms}$.

profile [26], [27], [31], [33]. The energy spectrum $E_{x'_s}$ is calculated using one-dimensional Fourier transform in the y or z direction, applied to $x_s(y,z;t)$. As x_s is statistically homogeneous on a y-z plane, the spectrum of x_s is expressed as a function of the transverse wavenumber k_t, whose direction is perpendicular to the x direction. Figure 3.9(b) shows the spectra of x'_s in the area-preserving form, $k_t E_{x'_s}(k_t)$. Here, k_t is normalized by the integral length scale of turbulence L. The profiles of $k_t E_{x'_s}$ have a peak value around $k_t L = 2$, and fluctuations in x_s are characterized by large scales. These energy spectra are similar to the pressure-jump-fluctuation spectra shown in Section 2.3.2. This indicates that large-scale turbulence motions affect the shock wave because of the dominant contribution of large scales to fluctuations in the shock wave.

All simulations are conducted using Re_λ of 60-70, and the differences between each case should be attributed to M_t and M_s. Previous studies characterized the shock–turbulence interaction using $M_t/(M_s-1)$ and $M_t^2/(M_s^2-1)$ [11], [26], [27], [31], [70]. Figure 3.10 plots $x'_{s,rms}/\eta$ against $M_t/(M_s-1)$ or $M_t^2/(M_s^2-1)$. All cases have $\eta/L_0 \approx$

0.012 because of the similar turbulent Reynolds number, and $x'_{s,rms}$ is divided by an almost constant value. Therefore, the figures are used to assess the relation between $x'_{s,rms}$ and $M_t/(M_s-1)$ or $M_t^2/(M_s^2-1)$, but not to assess the dependence on η. As mentined above, $x'_{s,rms}/\eta$ increases with M_t and decreases with M_s, and both $M_t/(M_s-1)$ and $M_t^2/(M_s^2-1)$ similarly change with M_t and M_s. However, the function $M_t^2/(M_s^2-1)$ better characterizes $x'_{s,rms}/\eta$ than $M_t/(M_s-1)$, as shown in Figure 3.10. In addition, $x'_{s,rms}/\eta$ exhibits a power law behavior of $M_t^2/(M_s^2-1)$, and the relation is obtained via the least squares method:

$$x'_{s,rms}/\eta \sim \left(\frac{M_t^2}{M_s^2-1}\right)^{0.46}. \tag{3.10}$$

For this relation, $x'_{s,rms}$ is almost proportional to M_t for fixed M_s; this is confirmed in Figure 3.10(a). As disscussed in Section 2.3.2, the rms values of the fluctuations of the pressure jumps, $\Delta p'_{rms}$, normalized by the mean pressure jump, $\overline{\Delta p}$, across the shock wave change with $\Delta p'_{rms}/\overline{\Delta p} \sim [M_t^2/(M_s^2-1)]^{0.46}$, whose exponent is same as Equation (3.10). A simplified argument of the shock-wave deformation [31], which successfully predicts power law behavior $\Delta p'_{rms}/\overline{\Delta p}$, shows that shock-wave deformation can cause pressure jump fluctuations. Shock-wave deformation is an appropriate measure of fluctuation in shock-wave strength because scaling exponents of the rms values of pressure jump fluctuations and shock-wave positions are very close. The power law of $\Delta p'_{rms}$ described in Section 2.3.2 and Ref. [31] is obtained from experimental and numerical data for both normal and spherical shock waves, and these shock waves rely similarly on $\Delta p'_{rms}$ on $M_t^2/(M_s^2-1)$. Considering the relation between shock-wave deformation and pressure jump fluctuations [31], the scaling law of $x'_{s,rms}$ is also expected to be valid in spherical shock waves with a large curvature.

As mentioned above, $x'_{s,rms}/\eta$ gradually increases with shock-wave propagation during turbulence. $x_s^{(\alpha)}$ is defined as the shock-wave position at which $x'_{s,rms}$ reaches $\alpha\%$ of the maximum value of $x'_{s,rms}$. The order of the time scale for the growth of $x'_{s,rms}$ can be roughly estimated as $t_s^{(\alpha)} = (x_s^{(\alpha)} - x_{s0})/U_s$. Although the present definition of $t_s^{(\alpha)}$ does not provide an exact time for the shock wave to be in a statistically stationary

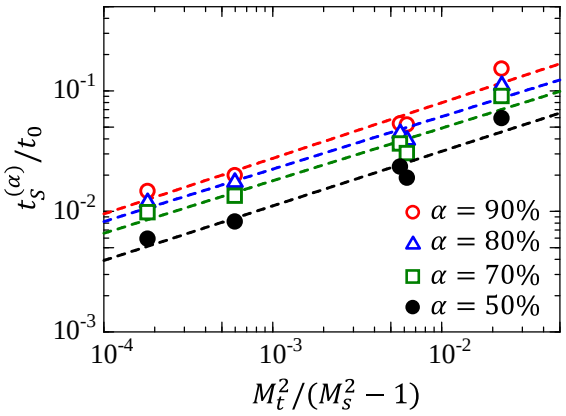

Figure 3.11. Time scales $t_s^{(\alpha)}$ of the growth of $x'_{s,rms}$ divided by t_0, plotted against $M_t^2/(M_s^2-1)$. Broken lines represent $t_s^{(\alpha)}/t_0 = A_t[M_t^2/(M_s^2-1)]^n$ obtained using the least squares method.

state, $t_s^{(\alpha)}$ is still useful when observing how the shock-wave deformation's time scale depends on M_s and M_t. $t_s^{(\alpha)}/t_0$ is plotted against $M_t^2/(M_s^2-1)$ for $50\% \leq \alpha \leq 90\%$ for all cases, as shown in Figure 3.11. Although $t_s^{(\alpha)}/t_0$ depends on α because of the definition, it generally increases with $M_t^2/(M_s^2-1)$. This trend may be explained by a time scale of the shock-wave deformation induced by velocity fluctuations, which can be estimated as $t_s = x'_{s,rms}/u_0$. The power law of $x'_{s,rms}$, Equation (3.10), can be read as $x'_{s,rms} \sim L_0[M_t^2/(M_s^2-1)]^{0.46}$ because L_0/η is almost constant due to the similar turbulent Reynolds number in all cases. Then, the following scaling law of a normalized time scale t_s/t_0 is obtained from an empirical relation of Equation (3.10):

$$t_s/t_0 \sim \left(\frac{M_t^2}{M_s^2-1}\right)^{0.46}. \tag{3.11}$$

This relation holds for the present DNS data in Figure 3.11: the least squares method yields exponents of the power law, written as $t_s^{(\alpha)}/t_0 = A_t[M_t^2/(M_s^2-1)]^n$, where $n = 0.46, 0.44, 0.44$, and 0.45 are obtained for $\alpha = 90\%, 80\%, 70\%$, and 50%, respectively. These values are close to 0.46, and Equation (3.11) is an adequate approximation of the time scale of shock-wave deformation at the interaction's initial transient process.

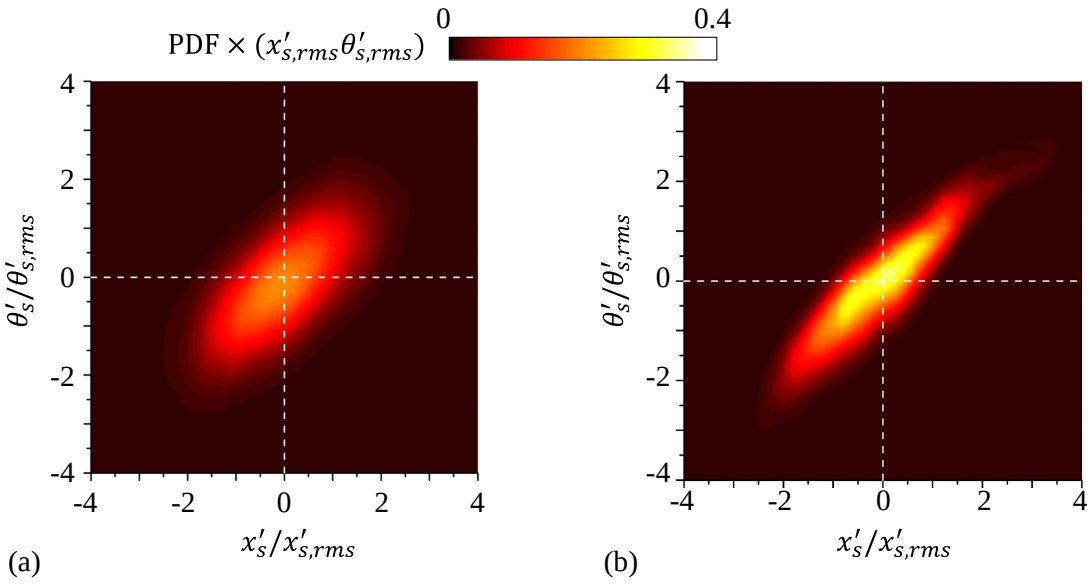

Figure 3.12. Joint PDFs between x'_s and θ'_s in (a) Case 3-1 and (b) Case 3-5.

3.3.3 Relation between local shock-wave characteristics and shock-wave position

Relations between local shock-wave characteristics and shock-wave deformation are investigated, where time instances with $13L_0 \leq \overline{x_s} \leq 19L_0$ are used in the same manner as with shock-wave deformation statistics. Dilatation, θ, evaluated at the shock-wave position, x_s, is denoted by $\theta_s(y,z;t) \equiv \theta(x_s,y,z;t)$. Figure 3.12 shows joint PDFs between x'_s and $\theta'_s \equiv \theta_s - \overline{\theta_s}$ in Cases 3-1 and 3-5, where $\overline{\theta_s}$ is the mean dilatation averaged in y and z directions. These quantities are positively correlated; that is, θ'_s tends to be positive when the shock wave is located in front of the mean shock-wave position, and vice versa. From the equation of mass conservation, the dilatation can also be represented as $\theta = -(1/\rho)(D\rho/Dt)$. The positive correlation between x'_s and θ'_s suggests that the shock wave with $x'_s < 0$ tends to have a stronger compression with a larger local shock Mach number. Because of the larger shock Mach number, the area of the shock wave behind the mean shock-wave position has a large propagation velocity, and x'_s approaches zero. Similarly, a shock wave area with $x'_s > 0$ has a smaller

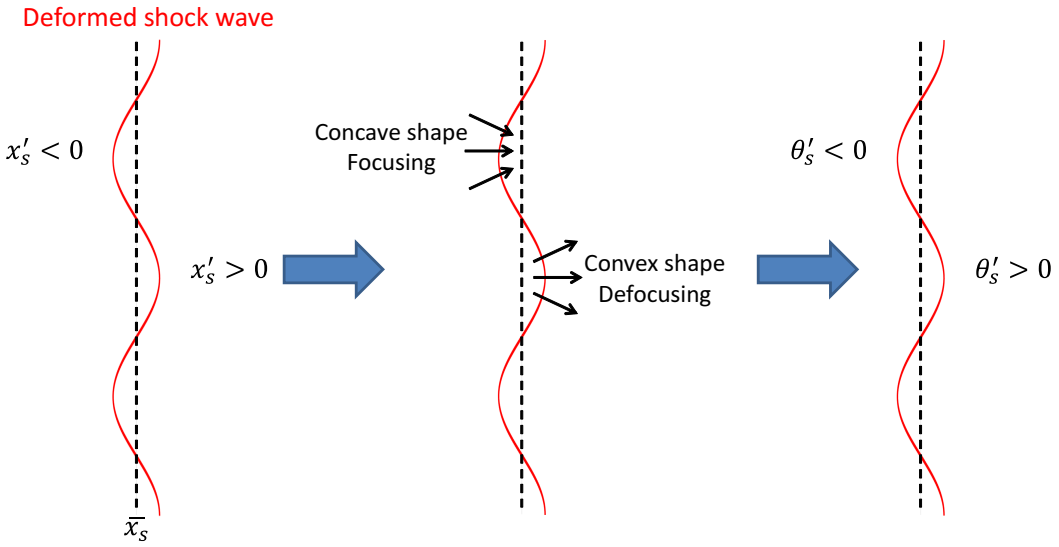

Figure 3.13. Conceptual picuture of the focusing and defocusing effects of the shock wave surface. The red solid line represents the deformed shock wave, while the black broken line represents the mean shock wave position.

propagation velocity than its average, and positive x_s' tends to decrease to 0. The stability of the shock surface against turbulence is explained by these relations between the shock-wave deformation and the local shock Mach number, whose conceptual picture is shown in Figure 3.13. The correlation between x_s' and θ_s' can be better explained by the relation between the curvature of the shock wave and the local strength of the shock wave, as also explained by Larsson *et al.* [27]. The focusing effect on a concave region amplifies the local shock Mach number [71], and the concave region is most likely to have a negative x_s'. A convex shape with the defocusing effect that weakens the shock wave is also likely to appear with $x_s' > 0$. These relations between the geometry of the shock-wave surface and the local shock-wave strength result in the positive correlation between x_s' and θ_s'.

The correlation coefficient between x_s' and θ_s' is calculated in all cases. Figure 3.14 plots the correlation coefficient $R_C = \overline{x_s'\theta_s'}/\left(x_{s,rms}'\theta_{s,rms}'\right)$ against $M_t/(M_s-1)$ or $M_t^2/(M_s^2-1)$. The influence of statistical convergence on R_C is discussed in the Appendix. The correlation coeffcients are positive in all cases and better characterized by $M_t/(M_s-1)$ unlike the case of $x_{s,rms}'$. In Cases 3-1 to 3-3, the correlation coefficients

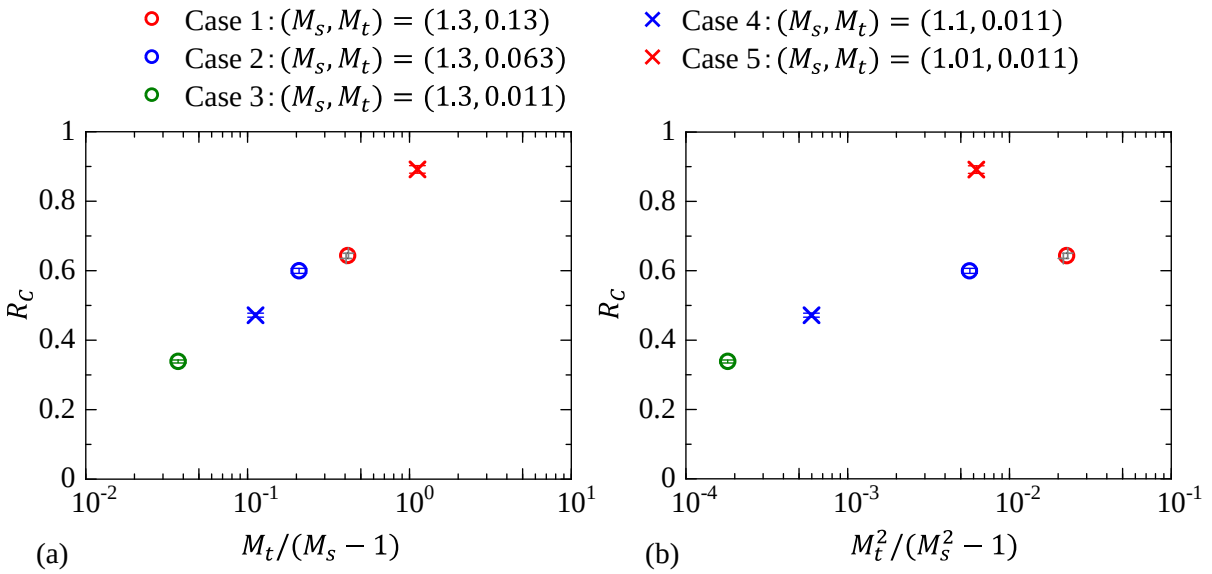

Figure 3.14. Correlation coefficients R_C between x_s' and θ_s' plotted against (a) $M_t/(M_s - 1)$ and (b) $M_t^2/(M_s^2 - 1)$. Gray "+" symbols are obtained by two independent sets of five simulations of Case 3-1. Error bars for Cases 3-2 to 3-5 represent 1.2% of the fractional error in R_C.

increase as the turbulent Mach number increases. Conversely, the correlation coefficients in Cases 3-3 to 3-5 increase in the presence of a smaller shock Mach number. In addition, the maximum and minimum correlations are observed in Cases 3-5 and 3-3, respectively. One of the possible reasons for dependence of R_C on the turbulent and shock Mach numbers is time lag effect of shock wave modulation descriebed in Section 2.3.4. Dilatation fluctuations at x_s are caused by turbulence that interacts with the shock wave before it reaches x_s. For a small M_t or a large M_s, the interaction that occurs before the shock wave reaches x_s rapidly affects the dilatation of the shock wave, and the correlation between x_s' and θ_s' can be weakened. In addition, a reason why the correlation coefficient R_C is maximized in Case 3-5 is its low turbulent Mach number. In Cases 3-3 to 3-5, dilatation is hardly fluctuated in turbulence because of the low turbulent Mach numbers. θ_s is hardly affected by the dilatation fluctuations of turbulence and dominated by compression in the shock wave in the cases. However, the turbulence effects on shock waves in Cases 3-3 and 3-4 relatively weaken because of high shock Mach numbers. Moreover, dilatation is fluctuated in turbulence in Cases 3-1

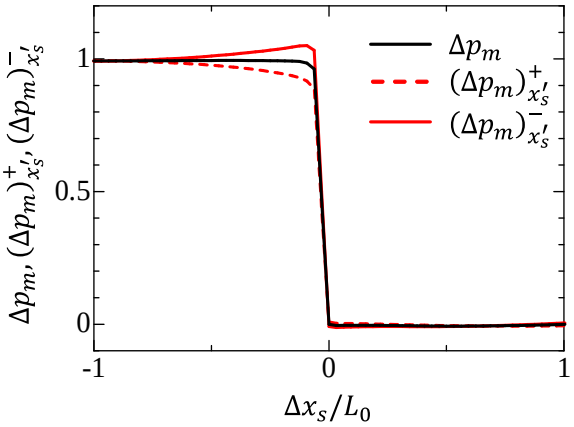

Figure 3.15. Mean pressure jumps Δp_m, $(\Delta p_m)^+_{x'_s}$, and $(\Delta p_m)^-_{x'_s}$ in Case 3-1. $(\Delta p_m)^+_{x'_s}$ and $(\Delta p_m)^-_{x'_s}$ are calculated for $x'_s > 0$ and $x'_s < 0$, respectively.

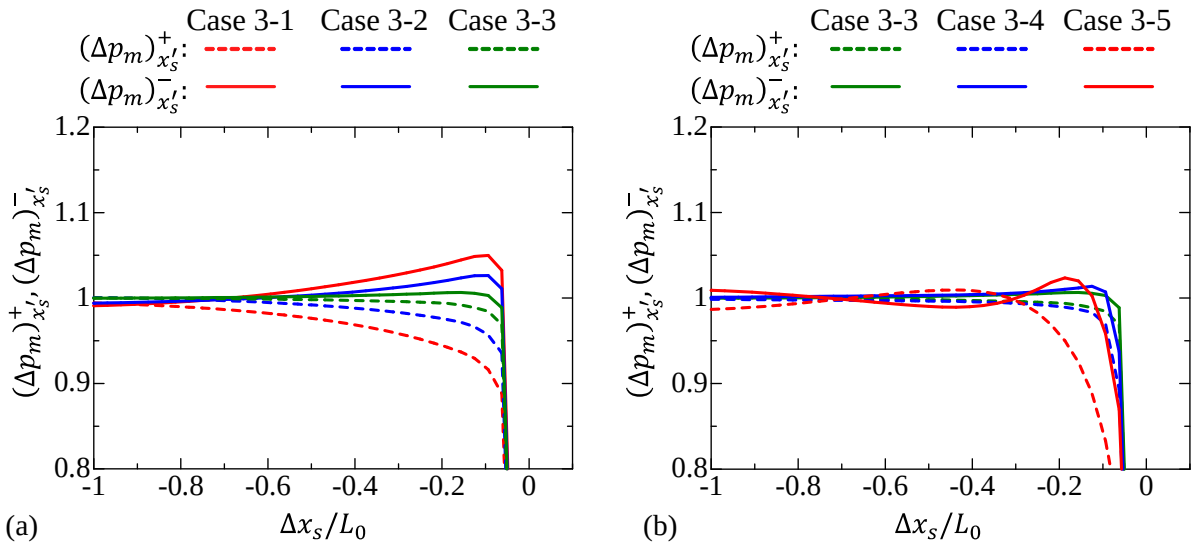

Figure 3.16. Mean pressure jumps obtained separately for $x'_s > 0$ and $x'_s < 0$, which are denoted by $(\Delta p_m)^+_{x'_s}$ and $(\Delta p_m)^-_{x'_s}$, respectively: (a) Cases 3-1 to 3-3; (b) Cases 3-3 to 3-5.

and 3-2 because their turbulent Mach numbers are relatively high. θ_s is affected by the dilatation fluctuations generated independently from the shock wave compression, and thus the correlation coefficient R_C shrinks in Cases 3-1 and 3-2. Note that these reasons why R_C is maximized in Case 3-5 can be applied to only the Cases 3-1 to 3-5. Further investigations are necessary to reveal the dependence of R_C on shock and turbulent Mach numbers.

The mean pressure jump across the shock wave is investigated, conditioned per the local distance from the shock wave in the x direction and defined as $\Delta x_s = x - x_s$. Its average conditioned on Δx_s is denoted by $\overline{f|\Delta x_s}$, which is calculated using a time average, averages in the y and z directions, and ensemble averages of five independent simulations. Here, the time average is taken for a time period with $13L_0 \leq \overline{x_s} \leq 19L_0$. The normalized mean pressure jump is defined as $\Delta p_m = (\overline{p|\Delta x_s} - p_F)/(p_B - p_F)$, similar to the local pressure jumps in Section 2.3.2, where p_B and p_F are the initial mean pressure behind and in front of the shock wave, respectively. With this definition, Δp_m is expected to change from 0 to 1 across the shock wave when an interaction does not occur. Dilatation within the shock wave represents the strength of the compression by the shock wave; therefore, x'_s should also be correlated with the pressure jumps across the shock wave. The relation between x'_s and the pressure jumps is assesed using the Δp_m, calculated separately for the shock-wave positions with $x'_s > 0$ and $x'_s < 0$, where the Δp_m calculated for $x'_s > 0$ and $x'_s < 0$ are denoted by $(\Delta p_m)^+_{x'_s}$ and $(\Delta p_m)^-_{x'_s}$, respectively. Figure 3.15 shows Δp_m, $(\Delta p_m)^+_{x'_s}$, and $(\Delta p_m)^-_{x'_s}$ in Case 3-1. As expected, the large pressure jumps for $x'_s < 0$ and the small pressure jumps for $x'_s > 0$ are found. Figures 3.16(a) and (b) show $(\Delta p_m)^+_{x'_s}$ and $(\Delta p_m)^-_{x'_s}$ in all cases, confirming the similar dependence of the mean pressure jump on x'_s. The difference between $(\Delta p_m)^+_{x'_s}$ and $(\Delta p_m)^-_{x'_s}$ grows as M_t increases in Figure 3.16(a) and M_s decreases in Figure 3.16(b).

Figure 3.16 shows that because the pressure jump amplifies when the shock wave is located behind the mean position, the profiles of $(\Delta p_m)^-_{x'_s}$ have a peak. The pressure-jump difference between $x'_s < 0$ and $x'_s > 0$ is evaluated as $(\Delta p_m)^-_{x'_s} - (\Delta p_m)^+_{x'_s}$ at the peak position of $(\Delta p_m)^-_{x'_s}$. As the shock wave tends to be strong and weak for $x'_s < 0$ and $x'_s > 0$, respectively, the difference in $(\Delta p_m)^-_{x'_s} - (\Delta p_m)^+_{x'_s}$ is a measure of the pressure-jump fluctuations normalized by the mean pressure jump. Figure 3.17(a) plots $(\Delta p_m)^-_{x'_s} - (\Delta p_m)^+_{x'_s}$ against $x'_{s,rms}$. The increase of $(\Delta p_m)^-_{x'_s} - (\Delta p_m)^+_{x'_s}$ with $x'_{s,rms}$ indicates that the pressure jump fluctuations become stronger with the shock-wave deformation. Figure 3.17(b) shows $(\Delta p_m)^-_{x'_s} - (\Delta p_m)^+_{x'_s}$ plotted against $M_t^2/(M_s^2 - 1)$. $(\Delta p_m)^-_{x'_s} - (\Delta p_m)^+_{x'_s}$ seems to be well characterized by $M_t^2/(M_s^2 - 1)$, similar to the case

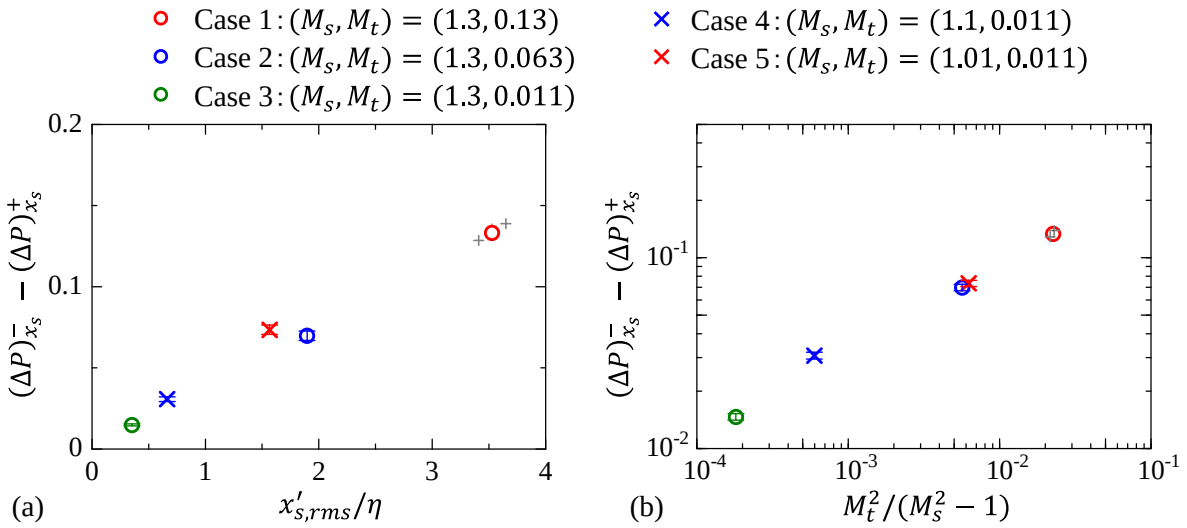

Figure 3.17. Difference between mean pressure jumps $(\Delta p_m)^+_{x'_s}$ and $(\Delta p_m)^-_{x'_s}$, which are calculated for $x'_s > 0$ and $x'_s < 0$, respectively. $(\Delta p_m)^-_{x'_s} - (\Delta p_m)^+_{x'_s}$ is evaluated at the position where $(\Delta p_m)^-_{x'_s}$ reaches a peak. The results are presented against (a) $x'_{s,rms}/\eta$ and (b) $M_t^2/(M_s^2-1)$. Gray + symbols are obtained by two independent sets of five simulations for Case 3-1. Error bars for Cases 3-2 to 3-5 represent 3.9% of the fractional error in $(\Delta p_m)^-_{x'_s} - (\Delta p_m)^+_{x'_s}$.

of x'_s. This result is consistent with the results disscussed in Chapter 2 and experimental studies [31], confirming that the rms value of the pressure jump fluctuations divided by the mean pressure jump rises with a power law of $M_t^2/(M_s^2-1)$.

Past experiments that assessed the interaction between a spherical shock wave and a turbulent jet used schlieren visualizations and pressure measurements to examine the link relationship between shock wave pressure jumps and geometry [28]. These studies showed that a shock wave with a concave shape in the propagation direction tends to have a large pressure jump. The concave shape forms when the shock-wave position is locally behind the mean shock-wave position; this experimental result is consistent with the present DNSs. In addition, a positive correlation was observed between the local shock-wave positions and the density jumps obtained via DNSs [27]. Previous experimental studies [30], [33] and the DNSs in Chapter 2 support the finding that velocity fluctuations during turbulence in the shock normal direction correlate with the pressure jump fluctuations. The fact that both turbulence velocity and the local shock-wave

positions are correlate with the pressure jumps suggests that shock-wave deformation is mainly caused by turbulence velocity fluctuations. The velocity of the shock-wave movement is defined as the sum of the velocity of the shock propagation and the flow velocity at local shock-wave positions, as explained in Section 2.3.4. The velocity of shock movements becomes non-uniform because of the turbulent velocity field. For example, velocity fluctuations in the opposite direction of the shock-wave propagation decrease the shock propagation velocity, resulting in a negative x'_s. Conversely, a positive x'_s is obtained via velocity fluctuations in the propagation direction. This relation between x'_s and velocity fluctuations can explain the correlation among x'_s, velocity, and jumps of pressure and density, as well as negative peak dilatation observed in experiments and numerical simulations. Shock-wave deformation can be also induced by temperature fluctuations during turbulence which in turn cause the speed of sound to fluctuate. This effect may be significant at very high turbulent Mach numbers, which are not considered in present DNSs.

3.3.4 Dissucussion about functions of $M_t/(M_s-1)$ and $M_t^2/(M_s^2-1)$

The functions of $M_t/(M_s-1)$ and $M_t^2/(M_s^2-1)$ are proposed independently to characterize the changes in physical quantities caused by a shock-turbulence interaction. Lee *et al.* introduced the fucntion of $M_t^2/(M_s^2-1)$ as a dominant parameter of broken shock wave [11]. They argued that the shock wave is broken when $M_t^2/(M_s^2-1) > 0.1$. Larsson *et al.* also explained that pressure fluctuations of turbulence is large compared to pressure jumps across a shock wave when $M_t^2/(M_s^2-1)$ is large [27]. Conversely, $M_t/(M_s-1)$ is introduced by Larsson *et al.* as a controlling parameter concerning the broken shock wave [27]. They defined a broken part of the shock wave as a part where a relative velocity of the fluid with respect to the shock wave on the shock wave surface is subsonic, and derived the function of $M_t/(M_s-1)$ based on the relative velocity. Therefore, the function of $M_t/(M_s-1)$ is related to momentum of turbulence and mean flow behind a shock wave, whereas the fucntion of $M_t^2/(M_s^2-1)$ is related to

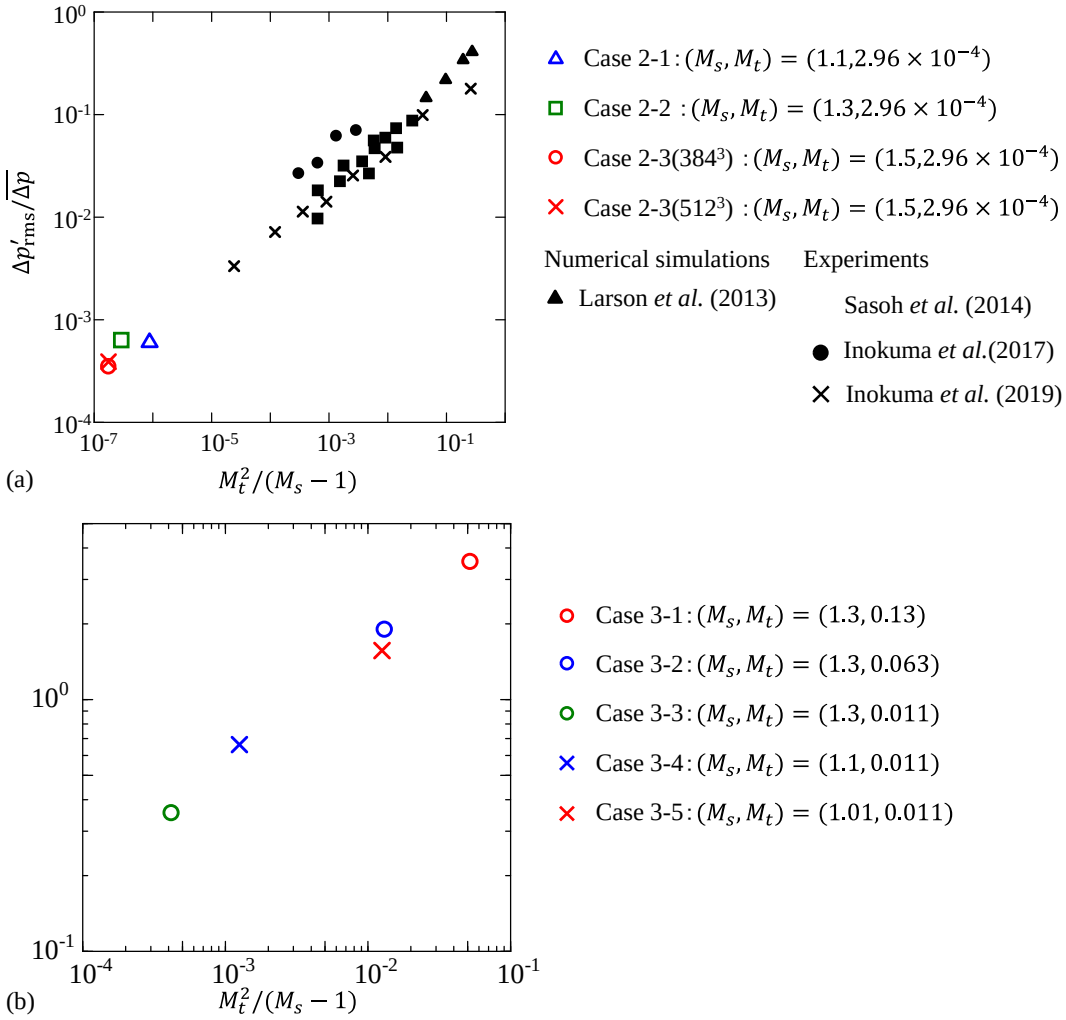

Figure 3.18. (a)$\Delta p'_{rms}/\overline{\Delta p}$ and (b)$x'_{s,rms}/\eta$ plotted against $M_t^2/(M_s-1)$.

energy of the turbulence and the flow induced by a shock wave. Figures 2.9 and 3.17 show that the pressure jump fluctuations are characterized by $M_t^2/(M_s^2-1)$ better than $M_t/(M_s-1)$. This implies that the pressrue jump fluctuations are directly influenced by dynamic pressure of turbulence in front of a shock wave. Similarly, the fluctuations of the shock-wave positions are also characterized by $M_t^2/(M_s^2-1)$ better than $M_t/(M_s-1)$. Therefore, the shock-wave deformation is also induced by dynamic pressure in turbulence. In addition, another possible function is $M_t^2/(M_s-1)$. Figures 3.18(a) and (b) plot $\Delta p'_{rms}/\overline{\Delta p}$ and $x'_{s,rms}/\eta$ against $M_t^2/(M_s-1)$, respectively. As a result, $\Delta p'_{rms}/\overline{\Delta p}$ and $x'_{s,rms}/\eta$ can be characterized by $M_t^2/(M_s-1)$ similar to $M_t^2/(M_s^2-$

1). This result also implies that the influences of dynamic pressure in turbulence are important for pressure jump fluctuations and shock-wave deformation.

3.4 Conclusions

The deformation of a normal shock wave from the transient process toward the stationary state of the shock–turbulence interaction is investigated via DNSs. The shock wave propagates from an initial quiescent region to a turbulent region, which is generated using HIT. Here, the shock Mach number M_s and turbulent Mach number M_t range between 1.01 and 1.3 and between 0.011 and 0.13, respectively, whereas the turbulent Reynolds number is 60 to 70 in all simulations. Most previous numerical studies on the shock–turbulence interaction have investigated a statistically stationary state of the interaction, which is achieved after the shock wave has propagated for a sufficiently long time. In this chapter's DNSs, the interaction's initial transition process can be investigated due to the setup, where the effects of the interaction gradually emerge on the shock wave. The local shock-wave position is identified by a local peak of the pressure gradient in the propagation direction. The shock-wave deformation's statistical properties are studied using the local shock-wave positions.

The following important characteristics of the shock-wave deformation are observed:

- The shock wave gradually deforms once it enters the turbulent region. Here, the rms value of the fluctuations of the shock-wave positions, $x'_{s,rms}$, increases with time, and it reaches a stationary state after the shock wave propagates in turbulence for a long time interval.
- The time scale of the shock-wave deformation's initial growth is well-characterized by the integral time scale t_0 of turbulence.

In the statistically stationary state of the interaction, the DNSs explained in this chapter revealed the following characteristics of the shock wave:

- $x'_{s,rms}$ increases with a power law of $M_t^2/(M_s^2-1)$, where the exponent of the

power law is 0.46 in the DNS used herein. This scaling exponent is similar to that obtained for the rms value of the fluctuations of the pressure jumps divided by the mean pressure jump obtained in Chapter 2 and an experimental study [31], which also increase with a power law of $M_t^2/(M_s^2-1)$.

- The Gaussian profile can be used effectively to approximate PDF fluctuations in the shock-wave position.
- The fluctuations in the shock-wave position are dominated by large-scale fluctuations , the length scale of which is similar to the turbulence's integral length scale.

The scaling of $x'_{s,rms}$ and the time scale of the shock-wave deformation's initial growth indicate that the duration of the initial transition process is proportional to $t_0[M_t^2/(M_s^2-1)]^{0.46}$.

The effects of shock-wave deformation on local shock-wave properties are investigated using dilatation and shock-wave pressure jumps. Dilatation, which represents the strength of compression, correlates with the fluctuations of the shock-wave positions; the correlation strengthens as $M_t/(M_s-1)$ increases. The sign of the correlation indicates that a backward-deforming shock wave tends to be strong, and vice versa. The mean pressure jump across the shock wave is calculated based on whether the shock wave deforms forward or backward. As expected from the correlation, an area with backward deformation tends to have a large pressure jump, whereas a smaller pressure jump appears for shock waves with forward deformation. The difference between the conditional mean pressure jumps under these two conditions increases with the rms value of the shock-wave position fluctuations and is represented well as a function of $M_t^2/(M_s^2-1)$.

Chapter 4

Conclusions

Shock-wave modulations induced by interactions with turbulence are investigated via DNSs of interaction between a normal shock wave and HIT. In the first simulations in Chapter 2, a normal shock wave interacts with HIT at a low turbulent Mach number, and the shock wave is hardly deformed. Conversely, a normal shock wave interacts with a local turbulent region in the second simulations in Chapter 3. This setup enables investigations of the transient process of shock-wave deformation. This was the first DNS study to examine this transient process.

In Chapter 2, DNSs of interactions between a normal shock wave and homogeneous isotropic turbulence whose turbulent Mach number is much lower than previous numerical simulations are performed, and statistical properties of pressure jump fluctuations in the shock wave and relationships between the pressure jump fluctuations and velocity fluctuations of turbulence normal to the shock wave are investigated. In addition, relationships between propagation directions of the local shock wave elements and velocity shear in turbulence are similar to the model introduced by Inokuma *et al.* [30]. The initial pressure jumps across the shock wave are defined based on Rankine-Hugoniot relations, and the interaction causes the local pressure jumps to fluctuate. The rms values of the pressure jump fluctuations are characterized by $M_t^2/(M_s^2-1)$. These fluctuations are negatively correlated with velocity fluctuations in the shock wave's normal direction. The negative correlation means that a pressure jump is amplified when the shock wave interacts with a velocity fluctuation opposite to the shock wave. The largest

negative correlation is located behind the shock wave, with the distance close to the longitudinal integral length scale of the turbulence. The location of the peak negative correlation implies the existence of a time lag until the shock wave is affected by the turbulence from the interaction. The time lag is explained by a model based on the shock-wave deformation induced by velocity fluctuations opposite to the shock wave [30]. Joint PDFs between the local propagation directions of the shock wave and the local velocity shear show positive correlations. Therefore, the local propagation direction of the shock wave is affected by turbulent shearing motions; those results are consistent with the model (Figure 2.11).

DNSs of a normal shock wave interacting with a local homogeneous isotropic turbulence are performed in Chapter 3. The initial transient process and statistically stationary state of shock-wave deformation are investigated via the DNSs. The transient process has been reported by Tamba *et al.* via only experiments of shadowgraph visualizations. Therefore, the quantitative investigation of the transient process is the most important originality of this study. Statistical properties of shock-wave deformation are investigated via the second DNS in Chapter 3. Shock-wave deformation is defined as fluctuations of local shock-wave positions. It begins once the shock wave enters the local turbulent region. The deformation reaches a stationary state after the shock wave propagates in the turbulent region for a long time interval. The time scale of the initial growth of the shock-wave deformation is characterized by the turbulence's eddy turnover time. The rms values of the fluctuations of the shock-wave positions $x'_{s,rms}$ are well characterized by $M_t^2/(M_s^2-1)$. The shock-wave positions are positively correlated with the dilatation in the shock wave, which represents the local strength of shock-wave compression. The correlation coefficient is characterized by $M_t/(M_s-1)$. The mean pressure jump across the shock wave is calculated conditioned on $x'_s > 0$ or $x'_s < 0$ as a function of distance from the local shock-wave position. The mean pressure jump with the condition $x'_s > 0$ shrinks, and vice versa. The difference between the conditional mean pressure jump under these two conditions increases with the rms values of the fluctuations of the shock-wave positions and is represented well as functions

of $M_t^2/(M_s^2 - 1)$.

Acknowledgments

I would like to thank my supervisor, Professor Koji Nagata. There is no doubt that I would not have been able to finish this work without his advice and comments. All of my communications with him supported my laboratory research. I am profoundly thankful for his understanding and thoughtful guidance.

My many discussions with Professor Akihiro Sasoh encouraged me and stimulated my intellectual curiosity. I was given several opportunities to discuss with him and members of his laboratory in research meetings about the shock–turbulence interaction. These discussions exposed me to countless valuable ways of thinking.

I would like to thank Professor Koichi Mori for his advice and questions during seminars in the laboratory. In addition, he let me join students' presentation practice. This enabled me to learn his way of thinking regarding presentation and education, and I was able to touch upon other research themes. It was a lot of fun to join the practice and discuss the student's presentations.

I really appreciate Professor Atsushi Matsuda for his helpful comments and questions while reviewing this thesis. I learned deeply from his feedback.

I am grateful to Doctor Tomoaki Watanabe, who gave me helpful advice during my study. He took a lot of time to allow me to discuss not only my research but also other research themes in the laboratory. It was these conversations that made me interested in fluid dynamics.

Professor Yasuhiko Sakai and Professor Yasumasa Ito gave me a lot of knowledge on turbulence. Discussions with them were one of the reasons why I became interested in studying not only shock waves but also turbulence. Professor Takeharu Sakai gave me

a lot of advice on numerical simulations. Doctor Akira Iwakawa taught me his way of thinking about education. I would also like to thank all my peers in the Fluid Dynamics Laboratory. Finally, I am deeply grateful to my family for their lifelong support.

I worked as a research fellowship at the Japan Society for the Promotion of Science (DC2) during my doctoral course. My research was supported by JSPS KAKENHI Grant No. 19J12973.

Finally, my simulations of the interaction between a normal shock wave and homogeneous isotropic turbulence were carried out under the Collaborative Research Project of the Institute of Fluid Science at Tohoku University. Direct numerical simulations of the time advancement of homogeneous isotropic turbulence were performed using the high-performance computing system supplied by the Japan Agency for Marine-Earth Science and Technology. Moreover, the direct numerical simulations of the normal shock wave interacting with a local turbulent region were performed using the high-performance computing system at Nagoya University.

Appendix : Effects of statistical convergence and spatial resolution

The effects of spatial resolution on the fluctuations of pressure jumps $\Delta p'$ and two-point correlation coefficients $C_{\Delta p',u'}$ shown in Chapter 2 are investigated using Case 2-3 with 384^3 and 512^3 grid points. It can be concluded that the grid spacing in the case of 384^3 is small enough to consider the pressure jumps because the profiles shown in Figures A.1(a) and A.1(b) are almost the same. This is why the results with 384^3 grid points are used in the DNSs of Chapter 2. In addition, spatial resolution hardly influences the results of $C_{\Delta p',u'}$, as demonstrated by the comparison between Figure A.2(a) and Figure A.2(b).

The effects of statistical convergence and spatial resolution on $x'_{s,rms}$ in Chapter 3 are investigated. The effects of the number of statistical samples are investigated for Case 3-1, for which 10 independent simulations are conducted using different snapshots of homogeneous isotropic turbulence. These 10 simulations are divided into two sets of five simulations, for which $x'_{s,rms}$ is calculated separately. Figure A.3(a) shows $x'_{s,rms}$ calculated from each set of all simulations. Three lines of $x'_{s,rms}$ are very similar. At the end of the simulation, the difference in $x'_{s,rms}$ between two sets of five simulations is 0.11η, which is much smaller than $x'_{s,rms}$. Therefore, the number of the samples does not affect the discussion on $x'_{s,rms}$. The statistical convergence of R_C is also checked using two independent sets of five simulations used in Figure A.3(a), for which $R_C = 0.65$ and

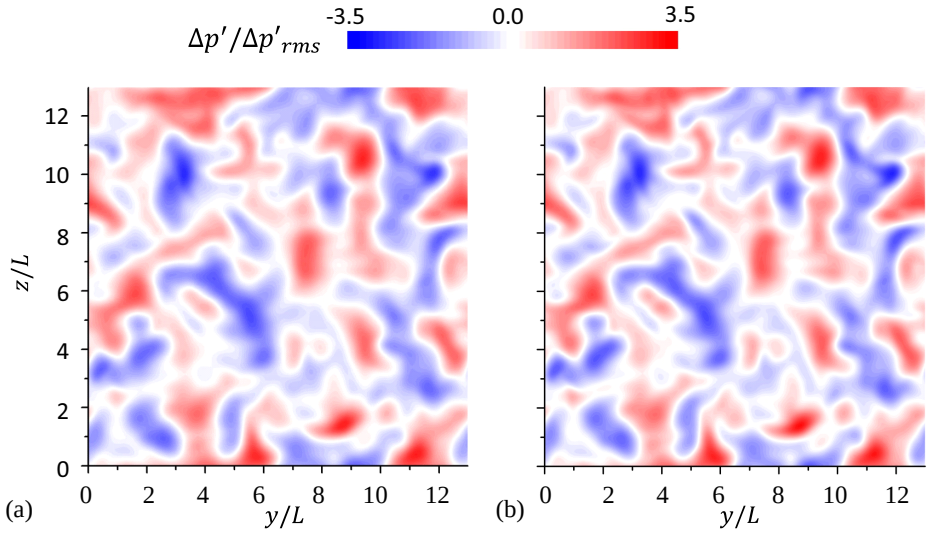

Figure A.1. Profiles of the fluctuations of normalized pressure jumps, $\Delta p'/\Delta p'_{rms}$, on the y-z plane at $x = x_p$: (a) Case 2-3 with 384^3 grid points, and (b) Case 2-3 with 512^3 grid points.

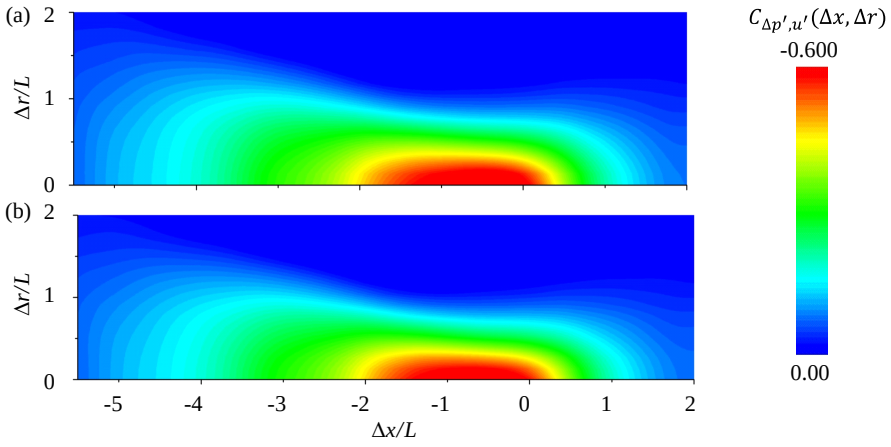

Figure A.2. Two-point correlation coefficients $C_{\Delta p',u'}(\Delta x, \Delta r)$ between the fluctuations of the pressure jumps across the shock wave, $\Delta p'(y, z; t)$, evaluated at $x_p(t)$, and the velocity fluctuations in the x direction of the initial HIT, $u'(\mathbf{x_p} + \mathbf{\Delta}; t = 0)$, where $\mathbf{x_p} = (x_p, y, z)$: (a) Case 2-3 ($384^3$ grid points), and (b) Case 2-3 (512^3 grid points).

0.64 are obtained. These results demonstrate that the number of samples barely affects the results of R_C presented in Figure 3.14. Conversely, the effects of spatial resolution on the analysis of $x'_{s,rms}$ are examined with additional simulations of the shock–turbulence interaction for $(M_s, M_t, Re_\lambda) = (1.3, 0.13, 20)$, whose Re_λ is smaller than that in the

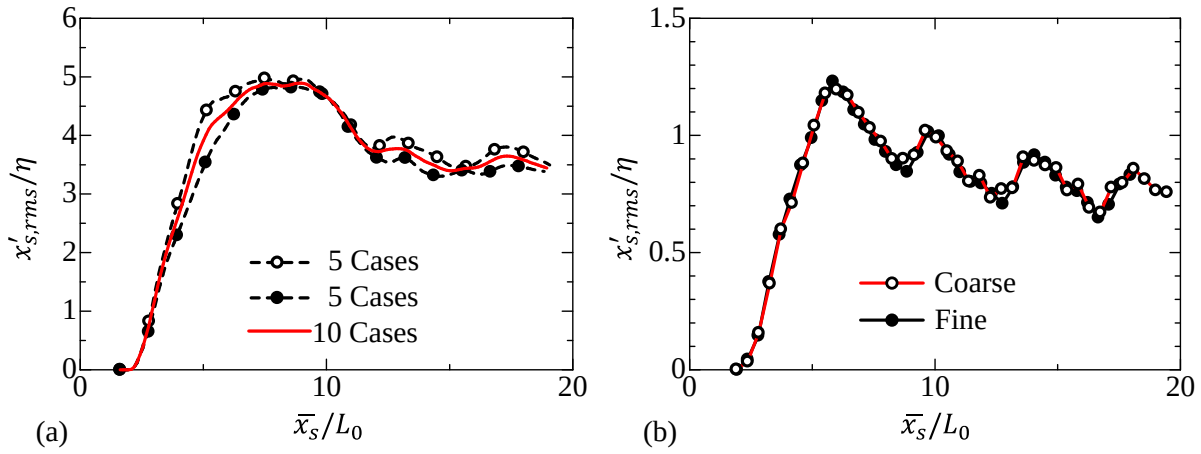

Figure A.3. (a) $x'_{s,rms}$ is calculated via two independent sets of five simulations of Case 3-1, where $x'_{s,rms}$ obtained from the 10 simulations is shown for comparison. (b) $x'_{s,rms}$ obtained from simulations with different spatial resolutions, where the fine and coarse cases have $\Delta/\eta = 0.34$ and 1.3, respectively.

other simulations. Simulations with a low Re_λ are performed with two grid settings. One uses fine grids with $(N_x, N_y, N_z) = (2048, 256, 256)$, while another uses coarse grids with $(N_x, N_y, N_z) = (512, 64, 64)$. For this Reynolds number, the grid sizes Δ/η are 0.34 and 1.3 for the fine and coarse grid settings, respectively. Here, the initial conditions are identical for the two simulations. Figure A.3(b) shows $x'_{s,rms}$ obtained using the fine and coarse grids. $x'_{s,rms}$ is hardly affected by the spatial resolution, confirming that the grid size $\Delta/\eta \approx 1.4$ is small enough to investigate statistics of x_s.

References

[1] C. B. Johnson and L. G. Kaufman. Interference heating from interactions of shock waves with turbulent boundary layers at mach 6. *NASA TN D-3074*, 1974.

[2] M.-M. Mac Low and R. S. Klessen. Control of star formation by supersonic turbulence. *Rev. Mod. Phys.*, 76(1):125, 2004.

[3] V. A. Thomas and R. J. Kares. Drive asymmetry and the origin of turbulence in an ICF implosion. *Phys. Rev. Lett.*, 109(7):075004, 2012.

[4] D. J. Maglieri. Some effects of airplane operations and the atmosphere on sonic-boom signatures. *The Journal of the Acoustical Society of America*, 39(5B):S36–S42, 1966.

[5] B. Tauzin, E. Debayle, C. Quantin, and N. Coltice. Seismoacoustic coupling induced by the breakup of the 15 february 2013 chelyabinsk meteor. *Geophys. Res. Lett.*, 40(14):3522–3526, 2013.

[6] C. Cerri. The effects of sonic boom on the ecological environment. *J. Navig.*, 33(2):296–303, 1980.

[7] M. Kanamori, T. Takahashi, Y. Makino, Y. Naka, and H. Ishikawa. Comparison of simulated sonic boom in stratified atmosphere with flight test measurements. *AIAA J.*, 56(7):2743–2755, 2018.

[8] J. Keller and W. Merzkirch. Interaction of a normal shock wave with a compressible turbulent flow. *Exp. Fluids*, 8(5):241–248, 1990.

[9] J. H. Agui, G. Briassulis, and Y. Andreopoulos. Studies of interactions of a propagating shock wave with decaying grid turbulence: velocity and vorticity fields. *J. Fluid Mech.*, 524:143–195, 2005.

[10] T. Kitamura, K. Nagata, Y. Sakai, A. Sasoh, and Y. Ito. Changes in divergence-free grid turbulence interacting with a weak spherical shock wave. *Phys. Fluids*, 29(6):065114, 2017.

[11] S. Lee, S. K. Lele, and P. Moin. Direct numerical simulation of isotropic turbulence interacting with a weak shock wave. *J. Fluid Mech.*, 251:533–562, 1993.

[12] S. Lee, S. K. Lele, and P. Moin. Interaction of isotropic turbulence with shock waves: effect of shock strength. *J. Fluid Mech.*, 340:225–247, 1997.

[13] D. Livescu and J. Ryu. Vorticity dynamics after the shock–turbulence interaction. *Shock Waves*, 26(3):241–251, 2016.

[14] R. Boukharfane, Z. Bouali, and A. Mura. Evolution of scalar and velocity dynamics in planar shock-turbulence interaction. *Shock Waves*, 28(6):1117–1141, 2018.

[15] C. H. Chen and D. A. Donzis. Shock–turbulence interactions at high turbulence intensities. *J. Fluid Mech.*, 870:813–847, 2019.

[16] Y. P. M. Sethuraman and K. Sinha. Effect of turbulent Mach number on the thermodynamic fluctuations in canonical shock-turbulence interaction. *Comput. Fluids*, 197:104354, 2020.

[17] H. S. Ribner. Shock-turbulence interaction and the generation of noise. *NACA Report No. 1233*, 1954.

[18] H. S. Ribner. Convection of a pattern of vorticity through a shock wave. *NACA Report No. 1164*, 1954.

[19] F. K. Moore. *Unsteady oblique interaction of a shock wave with a plane disturbance*, volume 1165. National Advisory Committee for Aeronautics, 1953.

[20] Y. P. M. Sethuraman, K. Sinha, and J. Larsson. Thermodynamic fluctuations in canonical shock–turbulence interaction: effect of shock strength. *Theor. Comput. Fluid Dyn.*, 32(5):629–654, 2018.

[21] N. O. Braun, D. I. Pullin, and D. I. Meiron. Large eddy simulation investigation of the canonical shock–turbulence interaction. *J. Fluid Mech.*, 858:500–535, 2019.

[22] Y. P. M. Sethuraman and K. Sinha. Modeling of thermodynamic fluctuations in canonical shock–turbulence interaction. *AIAA J.*, pages 1–14, 2020.

[23] L. Jacquin, C. Cambon, and E. Blin. Turbulence amplification by a shock wave and rapid distortion theory. *Phys. Fluids*, 5(10):2539–2550, 1993.

[24] K. Mahesh, S. K. Lele, and P. Moin. The response of anisotropic turbulence to rapid homogeneous one-dimensional compression. *Phys. Fluids*, 6(2):1052–1062, 1994.

[25] T. Kitamura, K. Nagata, Y. Sakai, A. Sasoh, and Y. Ito. Rapid distortion theory analysis on the interaction between homogeneous turbulence and a planar shock wave. *J. Fluid Mech.*, 802:108–146, 2016.

[26] J. Larsson and S. K. Lele. Direct numerical simulation of canonical shock/turbulence interaction. *Phys. Fluids*, 21(12):126101, 2009.

[27] J. Larsson, I. Bermejo-Moreno, and S. K. Lele. Reynolds-and Mach-number effects in canonical shock-turbulence interaction. *J. Fluid Mech.*, 717:293, 2013.

[28] J. H. Kim, A. Sasoh, and A. Matsuda. Modulations of a weak shock wave through a turbulent slit jet. *Shock Waves*, 20(4):339–345, 2010.

[29] A. Sasoh, T. Harasaki, T. Kitamura, D. Takagi, S. Ito, A. Matsuda, K. Nagata, and Y. Sakai. Statistical behavior of post-shock overpressure past grid turbulence. *Shock Waves*, 24(5):489–500, 2014.

[30] K. Inokuma, T. Watanabe, K. Nagata, A. Sasoh, and Y. Sakai. Finite response time of shock wave modulation by turbulence. *Phys. Fluids*, 29(5):051701, 2017.

[31] K. Inokuma, T. Watanabe, K. Nagata, and Y. Sakai. Statistics of overpressure fluctuations behind a weak shock wave interacting with turbulence. *Phys. Fluids*, 31(8):085119, 2019.

[32] K. Inokuma, T. Watanabe, K. Nagata, and Y. Sakai. Statistical properties of spherical shock waves propagating through grid turbulence, turbulent cylinder wake, and laminar flow. *Phys. Scr.*, 2019.

[33] K. Aruga, K. Inokuma, T. Watanabe, K. Nagata, and Y. Sakai. Experimental investigation of interactions between turbulent cylinder wake and spherical shock wave. *Phys. Fluids*, 32(1):016101, 2020.

[34] T. Tamba, G. Fukushima, M. Kayumi, A. Iwakawa, and A. Sasoh. Experimental

investigation of the interaction of a weak planar shock with grid turbulence in a counter-driver shock tube. *Phys. Rev. Fluids*, 4(7):073401, 2019.

[35] H. Tennekes. Intermittency of the small-scale structure of atmospheric turbulence. *Boundary-Layer Meteorol.*, 4(1-4):241–250, 1973.

[36] E. Johnsen, J. Larsson, A. V. Bhagatwala, W. H. Cabot, P. Moin, B. J. Olson, P. S. Rawat, S. K. Shankar, B. Sjögreen, H. C. Yee, et al. Assessment of high-resolution methods for numerical simulations of compressible turbulence with shock waves. *J. Comput. Phys.*, 229(4):1213–1237, 2010.

[37] S. B. Pope. *Turbulent Flows*. Cambridge Univ. Pr., 2000.

[38] G. Batchelor and A. Townsend. Decay of vorticity in isotropic turbulence. 190:534, 1947.

[39] G. Batchelor and A. Townsend. The nature of turbulent motion at large wave-numbers. 199(1057):238, 1949.

[40] R. W. Stewart. Triple velocity correlations in isotropic turbulence. *Proc. Camb. Phil. Soc.*, 47(1):146–157, 1951.

[41] R. M. Kerr. Higher-order derivative correlations and the alignment of small-scale structures in isotropic numerical turbulence. *J. Fluid Mech.*, 153:31–58, 1985.

[42] L. Mydlarski and Z. Warhaft. On the onset of high-Reynolds-number grid-generated wind tunnel turbulence. *J. Fluid Mech.*, 320:331–368, 1996.

[43] S. K. Lee, L. Djenidi, R. A. Antonia, and L. Danaila. On the destruction coefficients for slightly heated decaying grid turbulence. *Int. J. Heat Fluid Flow*, 43:129–136, 2013.

[44] T. Kitamura, K. Nagata, Y. Sakai, A. Sasoh, O. Terashima, H. Saito, and T. Harasaki. On invariants in grid turbulence at moderate Reynolds numbers. *J. Fluid Mech.*, 738:378–406, 2014.

[45] R. A. Antonia, S. L. Tang, L. Djenidi, and L. Danaila. Boundedness of the velocity derivative skewness in various turbulent flows. *J. Fluid Mech.*, 781:727–744, 2015.

[46] A. Y.-S. Kuo and Corrsin S. Experiments on internal intermittency and fine-structure distribution functions in fully turbulent fluid. *J. Fluid Mech.*, 50(2):285–

319, 1971.

[47] F. Ducros, F. Laporte, T. Souleres, V. Guinot, P. Moinat, and B. Caruelle. High-order fluxes for conservative skew-symmetric-like schemes in structured meshes: application to compressible flows. *J. Comput. Phys.*, 161(1):114–139, 2000.

[48] H. Saito. DNS of interaction of planar shock wave with homogeneous isotropic turbulence. *Master's thesis*, Nagoya University, 2013.

[49] G.-S. Jiang and C.-W. Shu. Efficient implementation of weighted ENO schemes. *J. Comput. Phys.*, 126(1):202–228, 1996.

[50] J. L. Ellzey, M. R. Henneke, J. M. Picone, and E. S. Oran. The interaction of a shock with a vortex: shock distortion and the production of acoustic waves. *Phys. Fluids*, 7(1):172–184, 1995.

[51] P. A. Davidson. *Turbulence: An Introduction for Scientists and Engineers.* Oxford Univ. Pr., 2004.

[52] G. B. Whitham. On the propagation of shock waves through regions of non-uniform area or flow. *J. Fluid Mech.*, 4(4):337–360, 1958.

[53] H. S. Ribner, P. J. Morris, and W. H. Chu. Laboratory simulation of development of superbooms by atmospheric turbulence. *J. Acoust. Soc. Am.*, 53(3):926–928, 1973.

[54] M. A. C. Teixeira and C. B. da Silva. Turbulence dynamics near a turbulent/non-turbulent interface. *J. Fluid Mech.*, 695:257–287, 2012.

[55] R. R. Taveira and C. B. da Silva. Characteristics of the viscous superlayer in shear free turbulence and in planar turbulent jets. *Phys. Fluids*, 26(2):021702, 2014.

[56] T. Watanabe, C. B. da Silva, K. Nagata, and Y. Sakai. Geometrical aspects of turbulent/non-turbulent interfaces with and without mean shear. *Phys. Fluids*, 29(8):085105, 2017.

[57] T. Watanabe, C. B. da Silva, Y. Sakai, K. Nagata, and T. Hayase. Lagrangian properties of the entrainment across turbulent/non-turbulent interface layers. *Phys. Fluids*, 28(3):031701, 2016.

[58] T. S. Silva and C. B. da Silva. The behaviour of the scalar gradient across the

turbulent/non-turbulent interface in jets. *Phys. Fluids*, 29(8):085106, 2017.

[59] K. Takamure, Y. Ito, Y. Sakai, K. Iwano, and T. Hayase. Momentum transport process in the quasi self-similar region of free shear mixing layer. *Phys. Fluids*, 30(1):015109, 2018.

[60] A. Jain and S. H. Kim. On the non-equilibrium models for subfilter scalar variance in large eddy simulation of turbulent mixing and combustion. *Phys. Fluids*, 31(2):025112, 2019.

[61] M. R. Petersen and D. Livescu. Forcing for statistically stationary compressible isotropic turbulence. *Phys. Fluids*, 22(11):116101, 2010.

[62] X. Zhang, T. Watanabe, and K. Nagata. Turbulent/nonturbulent interfaces in high-resolution direct numerical simulation of temporally evolving compressible turbulent boundary layers. *Phys. Rev. Fluids*, 3(9):094605, 2018.

[63] R. Nagata, T. Watanabe, and K. Nagata. Turbulent/non-turbulent interfaces in temporally evolving compressible planar jets. *Phys. Fluids*, 30(10):105109, 2018.

[64] Y. Tai, T. Watanabe, and K. Nagata. Modeling of molecular diffusion and thermal conduction with multi-particle interaction in compressible turbulence. *Phys. Fluids*, 30(3):035108, 2018.

[65] Z. Wang, Y. Lv, P. He, J. Zhou, and K. Cen. Fully explicit implementation of direct numerical simulation for a transient near-field methane/air diffusion jet flame. *Comput. Fluids*, 39(8):1381–1389, 2010.

[66] C. A. Kennedy and M. H. Carpenter. Several new numerical methods for compressible shear-layer simulations. *Appl. Numer. Math.*, 14(4):397–433, 1994.

[67] D. Gefroh, E. Loth, C. Dutton, and E. Hafenrichter. Aeroelastically deflecting flaps for shock/boundary-layer interaction control. *J. Fluids Struct.*, 17(7):1001–1016, 2003.

[68] F. Nicolas, V. Todoroff, A. Plyer, G. Le Besnerais, D. Donjat, F. Micheli, F. Champagnat, P. Cornic, and Y. Le Sant. A direct approach for instantaneous 3D density field reconstruction from background-oriented schlieren (BOS) measurements. *Exp. Fluids*, 57(1):13, 2016.

[69] L. D. Landau and E. M. Lifshitz. *Course of theoretical physics: Fluid mechanics*. Elsevier, 1987.

[70] D. A. Donzis. Shock structure in shock-turbulence interactions. *Phys. Fluids*, 24(12):126101, 2012.

[71] A. D. Pierce. Statistical theory of atmospheric turbulence effects on sonic-boom rise times. *J. Acoust. Soc. Am.*, 49(3B):906–924, 1971.